Article:
Chai, G, Webb, A, Li, C et al. (34 more authors) (2021) Mutations in Spliceosomal Genes PPIL1 and PRP17 Cause Neurodegenerative Pontocerebellar Hypoplasia with Microcephaly. Neuron, 109 (2). pp. 241-256. ISSN 0896-6273

https://doi.org/10.1016/j.neuron.2020.10.035

Mutations in spliceosomal genes *PPIL1* and *PRP17* cause neurodegenerative pontocerebellar hypoplasia with microcephaly

Guoliang Chai[1,13], Alice Webb[2,13], Chen Li[1], Danny Antaki[1], Sangmoon Lee[1], Martin W. Breuss[1], Nhi Lang[1], Valentina Stanley[1], Paula Anzenberg[1], Xiaoxu Yang[1], Trevor Marshall[1], Patrick Gaffney[3], Klaas J. Wierenga[4], Brian Hon-Yin Chung[5], Mandy Ho-Yin Tsang[5], Lynn S. Pais[6], Alysia Kern Lovgren[6], Grace E. VanNoy[6], Heidi L. Rehm[6], Ghayda Mirzaa[7], Eyby Leon[8], Jullianne Diaz[8], Alexander Neumann[9], Lars Kuhn[10], Arnout Kalverda[10], Iain Manfield[10], David A Parry[2], Clare V Logan[2], Colin Johnson[2], David T Bonthron[2], Elizabeth MA Valleley[2], Mohamed S Abdel-Hamid[11], Sherif F. Abdel-Ghafar[11], Mahmoud Y Issa[11], Patricia Jennings[12], Maha S. Zaki[11], Eamonn Sheridan[2]*, Joseph G. Gleeson[1,14]*

[1]Howard Hughes Medical Institute, Rady Children's Hospital, University of California San Diego, La Jolla, CA 92093, USA
[2]Clinical Genetics Department, Leeds Institute for Molecular Medicine, St James's Hospital, Leeds LS9 7TF, UK
[3]Genes and Human Disease Research Program, Oklahoma Medical Research Foundation, Oklahoma City, OK 73104, USA
[4] Department of Clinical Genomics, Mayo Clinic, Jacksonville, FL 32224, USA
[5]Department of Paediatrics and Adolescent Medicine, LKS Faculty of Medicine, U Hong Kong, SAR, China
[6]Broad Center for Mendelian Genomics, Broad Institute of MIT and Harvard, Cambridge, MA 02142, USA
[7]Center for Integrative Brain Research, Seattle Children's Research Institute, WA 98101, USA
[8]Department of Genetics and Metabolism, Children's National Medical Center, Washington DC 20010, USA
[9]Institute of Biology, Freie Universität Berlin, Berlin, 14195, German
[10]Astbury Centre for Structural Molecular Biology, U Leeds, Leeds, LS2 9JT, UK
[11]Clinical Genetics Department, National Research Centre, Cairo 12311, Egypt
[12]Department of Chemistry and Biochemistry, University of California, San Diego, La Jolla, CA 92093, USA
[13]These authors contributed equally
[14]Lead Contact
*Correspondence: e.sheridan@leeds.ac.uk (E.S.), jogleeson@ucsd.edu (J.G.G.)

SUMMARY

Autosomal-recessive cerebellar hypoplasia and ataxia comprise a group of heterogeneous brain disorders, caused by disruption of several fundamental cellular processes. Here, we identified 10 families showing a neurodegenerative condition involving pontocerebellar hypoplasia with microcephaly (PCHM). Patients harbored biallelic, mutations in genes encoding the spliceosome components Peptidyl-Prolyl Isomerase Like-1 (PPIL1) or Pre-RNA Processing-17 (PRP17). Mouse knockouts of either gene were lethal in early embryogenesis, whereas *PPIL1* patient mutation knockin mice showed neuron-specific apoptosis. Loss of either protein impacted splicing integrity, predominantly affecting short and high GC-content introns and genes involved in brain disorders. PPIL1 and PRP17 form an active isomerase-substrate interaction, however, we found isomerase activity is not critical for function. Thus, we establish disrupted splicing integrity and 'major spliceosome-opathies' as a new mechanism underlying PCHM and neurodegeneration, and uncover a non-enzymatic function of a spliceosomal proline isomerase.

KEYWORDS: Pontocerebellar hypoplasia, microcephaly, neurodegeneration, brain development, spliceosome, cyclophilin, proline isomerase, alternative splicing, PCHM, PPIL1, PRP17, NMR, recessive disease

Abstract word count: 137, Manuscript word count: 3931, Tables: 1, Figures: 6 + 7, Supplemental tables: 5, Movie: 1

HIGHLIGHTS

- Mutations in two spliceosomal genes, *PPIL1* and *PRP17*, are identified in human autosomal-recessive pontocerebellar hypoplasia with microcephaly
- *PPIL1* or *PRP17* knockout mice show early embryonic lethality
- *PPIL1* patient mutation knockin mice show defective brain development with dramatic neuron-specific apoptosis
- Loss of *PPIL1* or *PRP17* disrupts RNA splicing integrity, particularly for introns with short length and high GC content and genes involved in brain disorders
- PPIL1 engages PRP17 Gly94-Pro95 bond and can catalyze cis-trans isomerization in vitro
- Catalysis of PRP17 isomerization by PPIL1 is not critical for splicing and neuronal survival

INTRODUCTION

Pontocerebellar hypoplasia (PCH) refers to a group of severe pediatric-onset neurodegenerative disorders affecting cellular survival in the brainstem and cerebellum, resulting in impaired neurological function and early death (Cassandrini et al., 2010). Humans with PCH show near-normal early embryologic development, followed by mid-gestational slowing or cessation and later regression in select neuroanatomical regions (Joseph et al., 2014). Most genes implicated in PCH are involved in tRNA splicing or GTP availability, suggesting a potential effect on protein translation (Breuss et al., 2016; Budde et al., 2008; Karaca et al., 2014; Schaffer et al., 2014). While postnatal progressive microcephaly can be part of the clinical spectrum, children are mostly born with normal or only mildly reduced head circumference (van Dijk et al., 2018).

Pre-mRNA splicing, mediated by the spliceosome complex, is essential for gene expression and regulation in higher organisms (Shi, 2017; Will and Luhrmann, 2011). Increased splicing complexity results in dramatically enlarged diversity in both the transcriptome and proteome: for instance, 95% of multi-exon human genes undergo alternative splicing (AS). Not surprisingly, AS is especially prevalent in the brain, corresponding to its complex composition of cell types and functions (Raj and Blencowe, 2015; Zhang et al., 2016). Remarkably, while aberrant splicing of individual genes due to defective cis- or trans-regulation has been widely reported in human brain diseases, global splicing defects by mutations in core major spliceosome complex (MSC) components have rarely been associated (Chabot and Shkreta, 2016; Scotti and Swanson, 2016).

Incorporated within the MSC are eight cyclophilin peptidyl-prolyl isomerases (PPIase), enzymes initially found as targets of immunosuppressants, but later found to promote conformational changes of substrates by catalyzing cis-trans isomerization of Xaa-Proline peptide bond (Davis et al., 2010; Evans et al., 1987; Rajiv and Davis, 2018; Teigelkamp et al., 1998; Zhou et al., 2002). Functions and substrates of most PPIases remain unknown. Here, we report that biallelic, hypomorphic mutations in two spliceosomal genes *PPIL1* and *PRP17*, encoding an active PPIase-substrate pair, disrupt RNA splicing integrity and cause converging neurodegenerative phenotypes in human and mouse. While both proteins are required for spicing integrity and neuronal survival, surprisingly, mutations preventing PRP17 isomerization catalyzed by PPIL1 are tolerated, thus revealing a predominant non-enzymatic function of a spliceosomal PPIase.

RESULTS

Identification of biallelic mutations in *PPIL1* in PCHM families

From our cohort of 7,288 patients with recessive congenital neurological disorders, we identified rare damaging homozygous missense variants in *PPIL1* among 8 index cases from 5 families (Figures 1A–1C). All patients showed both features of PCH as well as congenital microcephaly (-3SD to -6SD HC); the latter phenotype progressed postnatally for all. Patients did not show features of known syndromic PCH subtypes (Akizu et al., 2013; Namavar et al., 2011) (Table 1 and Table S1). All subjects were enrolled with IRB-approved protocols at referral institutions and provided signed consent. Through Genematcher (Sobreira et al., 2015), we identified 4 additional families with 8 affected patients in which *PPIL1* mutations were independently identified as the likely cause (Table S1 and S2). As all individuals exhibited PCH with microcephaly, we defined this

presentation as a unique clinical entity, which we termed PCHM (PCH+Microcephaly). Further common phenotypes included hypotonia, difficulty swallowing, failure to control the airway, seizures, and delayed motor and language development. Brain MRI showed cortical changes in most affecteds (Figure 1B and Table S1), notably simplified gyri pattern, which was rarely reported for other subtypes of PCH.

The mutations in each family segregated with the phenotype according to recessive inheritance. Families 1-5 showed homozygous missense variants, and Family 6 showed two separate homozygous variants predicting a 6 aa duplication and a p.G109C substitution. Family 7-9 showed compound heterozygous variants: Families 5 and 7 and Family 8 and 9 shared an identical variant. All substituted residues were highly conserved (Figure S1A), predicted 'damaging' by MutationTaster (Schwarz et al., 2014), and clustered within PPIL1's cyclophilin PPIase domain, suggesting deleterious functions (Figure 1C).

Patient mutations affect PPIL1 function

PPIL1 joins the MSC together with its interacting protein SKIP, two of the NineTeen complex-related proteins, during B complex formation, and remains until splicing is complete (Rajiv and Davis, 2018; Wang et al., 2010). We mapped human mutations onto the ordered globular PPIL1 structure (Xu et al., 2006), and found all the affected residues except p.R131 were located on the enzymatic face (Figure 1D). To test the impacts of patient variants, we expressed FLAG-tagged mutant protein in HEK293T cells and found most variants led to unstable proteins (Figures S1B and S1C). Specifically, p.Y78C, p.A99T, p.[A101_D106dup;G109C], p.F82S and to a lesser degree p.T127A were barely detectable. Reduced endogenous p.A99T PPIL1 protein but not RNA was also observed in patient fibroblasts (Figures S1D–S1F).

Two variants, including p.T107A and p.R131Q, did not show altered protein levels in HEK293T cells. However, we found that both purified mutant proteins showed reduced thermal stability and increased aggregation propensity (Figures S1G–S1I). PPIL1 associates with SKIP prior to its incorporation into the spliceosome (Wang et al., 2010; Xu et al., 2006). The SKIP binding interface is located on the non-enzyme face (Wang et al., 2010; Xu et al., 2006), and previous studies suggested that PPIL1 p.R131 was involved in the binding to SKIP (Wang et al., 2010; Xu et al., 2006). As expected, we found that purified p.R131Q PPIL1 failed to associate with SKIP in both surface plasmon resonance and immunoprecipitation assays (Figures S1J and S1K). PPIL1 p.T107A, although localized to the enzymatic face, showed reduced SKIP interaction (Figure S1J). Thus, all assessed PPIL1 patient mutations either affect protein stability or interaction with SKIP.

Defective brain development and neuron-specific apoptosis in knockin mice

To reveal functions of PPIL1 in brain development, we studied expression during development. RNA *in situ* hybridization showed ubiquitous *Ppil1* expression in the developing cortex (Figures 2A and 2B). Due to a lack of specific PPIL1 antibodies, we generated a CRISPR knockin mouse introducing an N-terminal HA epitope in *Ppil1*, which confirmed ubiquitous protein expression (Figures 2C, 2D, and S2A–S2D). We next generated a *Ppil1* frameshift mouse line (*fs*, c.302delC, p.N102Tfs*13), but found no viable homozygous embryos any time after embryonic day (E) 12.5 (0 in 41 embryos, *p*

< 0.00001, Binomial test), while *Ppil1*$^{fs/+}$ pups were indistinguishable from wild-type (WT) littermates. However, at E9.5 we recovered several partially resorbed embryos, all of which were genotyped as *Ppil1*$^{fs/fs}$ (13 mutants in 46 embryos, with the expected 25%, Figures 2E and S2E). We conclude that *Ppil1* is essential for embryogenesis.

We next generated a patient p.A99T knockin (KI) mouse line, chosen because it was the first allele we identified. *Ppil1*$^{A99T/A99T}$ mice were born at the expected Mendelian ratios (22 *Ppil1*$^{A99T/A99T}$, 42 *Ppil1*$^{A99T/+}$, and 23 WT), but died within 24h. Newborns showed smaller head size, severely reduced cerebral and cerebellar size, reduced cortical surface area and thickness (Figures 2F–2M), matching human PCH phenotypes. While the cortex showed normal lamination, neuronal numbers were severely reduced, with CUX1$^+$ upper layer neurons decreased by ~25% and CTIP2$^+$ deep layer neurons by ~60% (Figures 2N and 2O). Like patient fibroblast, PPIL1 protein was also severely reduced by ~80% in *Ppil1*$^{A99T/A99T}$ embryo lysates (Figures S2F and S2G). Additionally, compound heterozygous *Ppil1*$^{A99T/fs}$ mutant embryos showed much more severe phenotypes across the body at E18.5 (Figure S2H), suggesting that *PPIL1* p.A99T is a hypomorphic mutation.

Based on the severe reduction in cortical thickness and neuronal numbers, we hypothesized that this could be caused by cell death during embryonic development. We examined apoptosis by assessing cleaved caspase 3 (CC3) and p53 expression in the embryonic brains. Indeed, the apoptosis showed a striking accumulation in TUJ1$^+$ neurons within deep layers of the lateral cortical margin in the mutant brains starting at E12.5 and dramatic at E14.5 (Figures 3A–3F), with some apoptotic cells are GAD65/67$^+$ interneurons (Figures S2I and S2J). The apoptosis in the rest of the cortex appeared at E14.5 and turned to be massive at E16.5 (Figures 3A–3N). Apoptotic cells predominantly localized in the cortical plate and did not overlap with SOX2$^+$ neural stem cells (NSCs) and TBR2$^+$ intermediate neural progenitors (INPs) (Figures 3G–3N and S2K–S2M). ~70% of p53 positive cells were positive for CTIP2 and ~30% for CUX1, consistent with a more severe reduction of deep layer neurons. CC3 upregulation was also observed in the cerebellum and pons at E18.5 (Figure S2N and S2O). Consistent with the predominant impact of the brain in the patients and KI mutant mice, no significant upregulation of apoptosis was observed in other major organs (Figures S2P and S2Q).

Recent studies proposed MSC defects result in genome instability, due partially to accumulated R-loops, transient RNA:DNA hybrid structures that displace the non-templated strand and generate susceptibility to DNA damage (Jangi et al., 2017; Paulsen et al., 2009), evidenced by γ-H2AX and p53 accumulation (Denis et al., 2005; Sorrells et al., 2018). Like p53, we indeed observed a dramatic upregulation of γ-H2AX in the mutant brains (Figures 3M, 3N, and S2L), suggesting similar mechanisms.

In contrast to other genetic models of microcephaly (Gruber et al., 2011; Insolera et al., 2014; Silver et al., 2010), no premature neurogenesis was observed at E12.5 (Figures S3A and S3B), and apoptosis initiation through p53 was predominantly localized to postmitotic neurons but not neural progenitors; consequently, the numbers of both neural stem cells (NSCs) and intermediate progenitors (INPs) only showed a slight reduction (Figures 3O–3X). The cell cycle of the mutant progenitors seems not to undergo dramatic alterations, as we only observed a slightly increased percent of INPs at the G2/M phase (Figures S3C–S3F). Together, our results suggest genotoxic stress, neuronal apoptosis, and perturbations of progenitors lead to brain volume loss in *Ppil1* KI mutants.

PPIL1 is required for alternative splicing integrity

Despite its discovery in the spliceosome many years ago (Rappsilber et al., 2002), the function of PPIL1 in RNA splicing remains mostly unknown. Since *Ppil1*$^{fs/fs}$ embryos survived until E9.5, we suspected that some cells might tolerate a complete loss of *PPIL1*. Thus, we generated *PPIL1* knockout (KO) human HAP1 cells (Figure S4A), which were viable and subjected to RNA-seq. Five different forms of alternative splicing (AS), including skipped exons (SE), mutually exclusive exons (MXE), alternative 5' and 3' splice sites selection (A5SS and A3SS), and retained introns (RI), were evaluated using rMATS software (Shen et al., 2014). We benchmarked rMATS by comparing variation within groups of 3 controls *vs.* 3 controls, where a baseline of 4,045 (i.e. 1.7%) significant differential splicing events (SDSE) were identified from 231,850 total AS events (Table S3). In contrast, 8,602 (i.e. 3.4%) SDSEs were identified comparing 3 KOs *vs.* 3 controls, with the number of SDSEs scaling with number replicates in each group (Figures S4B and S4C). We repeated the computational analysis using LeafCutter (Li et al., 2018), which identified 951 SDSEs between 3 KO *vs.* 3 controls, compared with 8 and 0 SDSEs for 3 controls *vs.* 3 controls vs. 3 KO *vs.* 3 KO (Table S3), respectively. All these revealed a dramatic disruption of global AS integrity upon loss of PPIL1.

We also confirmed altered AS by assessing 'sashimi-plot pile-ups' of RNAseq and performing RT-PCR validation on selected RI and SE events (Figures S4D–S4H). Loss of PPIL1 predominantly impacted the splicing of short and high GC-content introns, without significant bias towards splice site strength (Figures S4I–S4M). The most severe changes were present in introns ≤ 75 bp in length and with > 70% GC content (Figures S4N and S4O), where 12.6% of such introns were retained at higher levels in KO cells, compared with only 0.66% higher in controls.

Finally, we compared the list of SDSE genes in KO with OMIM disease categories based upon organ system involved and found overrepresentation for neurodevelopmental disease ($p = 3.45 \times 10^{-20}$, Bonferroni corrected Chi-squared test, Figure S4P), but not for cancer, cardiac or immune disease ($p > 0.05$). We also found that SDSE genes were significantly enriched in genes known to undergo AS in the brain ($p = 1.12 \times 10^{-287}$, Figure S3L). All these findings are consistent with its predominant impact on the brain.

Disrupted alternative splicing integrity in *Ppil1*$^{A99T/A99T}$ brains

To test the impact of its loss on AS integrity in the brain tissue, we performed RNAseq on 3 WT and 3 *Ppil1*$^{A99T/A99T}$ KI E14.5 brains before the accumulation of apoptotic cells. Using rMATS, we detected 3,797 SDSE among 236,870 total AS events (i.e. 1.6%, Figures 4A and S5A–S5C). Splicing alterations were also confirmed with Leafcutter, which identified 115 SDSE of 16,528 total AS events (i.e. 0.7%). A randomly selected group of significant RI and SE events were verified in semi-quantitative RT-PCR (Figures S5D and S5E). Two 'minigene' constructs transfected into MEFs for the SDSE introns of *Atg4d* and *Evi5l* confirmed that the splicing defects were not secondary to non-specific effects (Figures 4B and S5F). Similar to HAP1 cells, KI brains showed significant RI events for short and high GC-content introns (Figures 4C and 4D). However, unlike HAP1 KO cells, we also observed a preference for weak 5' and 3' splicing sites among significant events (Figures 4E–4H and S5G), which may reflect competition for reduced PPIL1 protein between strong and weak splicing sites. Profiling of misspliced genes revealed protein translation, RNA processing, and DNA damage response as the most significantly disturbed modules

(Figures 4I, S5H, and S5I), whose disruptions are major causes of cerebellar ataxia (Synofzik et al., 2019). Moreover, genes involved in axon development and cell cycle were also significantly affected (Figure 4I), reinforcing the phenotypes observed in KI brains.

PPIL1 catalyzes the isomerization of PRP17 Gly94-Pro95 *in vitro*

Recent cryo-EM structures allowed for detailed analysis of proline isomerases within the MSC (Bertram et al., 2017; Fica et al., 2019; Haselbach et al., 2018; Yan et al., 2015a; Zhan et al., 2018a; Zhang et al., 2017; Zhang et al., 2018; Zhang et al., 2019), six of which were evident in one or more MSC complexes (Table S4). However, only for PPIL1 was it possible to identify a Pro from an adjacent protein within the enzymatic pocket, where we identified Gly94-Pro95 of PRP17 within the B^{act}, C, C*, P, and ILS complexes (Fica et al., 2019; Zhan et al., 2018a; Zhang et al., 2017; Zhang et al., 2018; Zhang et al., 2019), conserved from *S. pombe* (Yan et al., 2015a) to human (Figures 5A, 5B, and S6A–S6E). This finding suggests that PRP17 may be a substrate of PPIL1 in the MSC.

Gly94-Pro95 in PRP17 occurs within an intrinsically unstructured region, between two alpha-helical domains, conserved from *S. pombe* to human (Figure 5C). There is an adjacent residue (human Phe93 or *S. pombe* Leu67) within the S2 pocket, which likely determines substrate specificity (Davis et al., 2010; Teigelkamp et al., 1998). To test their interaction, we performed heteronuclear single-quantum coherence (HSQC) spectral analysis with ^{15}N-labeled PPIL1, and a 13-mer PRP17 peptide (aa 89-101) containing Pro95. We confirmed that PRP17 peptide interacts with PPIL1 along its enzymatic surface (Figures 5D–5F). Using isothermal titration calorimetry assay, we defined a dissociation constant (K_D) of 111.9 ± 4.0 μM (Figure S6F). To investigate whether PPIL1 catalyzes PRP17 isomerization, we used a PRP17 peptide (aa 89-101) with ^{15}N, ^{13}C double-labeled P95, and demonstrated the Gly94-Pro95 bond was present in both cis and trans conformations (Figures S6G and S6H). Addition of catalytic concentrations of PPIL1 accelerated the rate of proline isomerization in PRP17 peptide, evidenced by the appearance of exchange peaks in ^{1}H ^{15}N H(Cα)N ZZ exchange spectra (Figures 5G–5I). This was also confirmed using 2D ^{1}H-^{15}N ZZ exchange spectra of a uniformly ^{15}N labeled PRP17 peptide (aa 84-101) with catalytic concentrations of PPIL1 WT (Figure S6I). We conclude that PPIL1 is capable of catalyzing PRP17 isomerization *in vitro*.

***PRP17* loss associates with pontocerebellar hypoplasia**

Only a few of the >100 MSC components are associated with human disease (Lines et al., 2012; Pellagatti and Boultwood, 2017; Ruzickova and Stanek, 2017; Xu et al., 2017), so we considered genes encoding PPIL1-associated proteins as candidates for PCHM. In addition to PRP17, we found SKIP and RBM22 bound to PPIL1 (Figures S6A–S6C and Movie S1). We thus searched our unsolved pediatric brain disease cases and identified a multiplex consanguineous family with PCHM (Family 10), also with chronic anemia and thrombocytopenia, and with a homozygous *PRP17* variant, predicting a damaging p.F502C protein change (Figures 6A, 6B, and Table S1 and S2). No further families were identified in Genematcher.

PRP17 contains a C-terminal WD40 domain, where F502 resides, which is fully evolutionarily conserved (Figures 6C and 6D). In cryo-EM MSC structure, the WD40 assumes a classical ‘7-propeller’ architecture, and associates with U2 snRNA and the

U2/branch point sequence (BPS) duplex, stabilizing the catalytic site (Movie S1) (Bertram et al., 2017; Haselbach et al., 2018; Zhan et al., 2018a; Zhang et al., 2017). We assessed the impact of p.F502C on protein using HA-tagged cDNA expressed in HEK293T cells and found dramatic protein destabilization, which was also confirmed in patient fibroblasts (Figures 6E–6G and S7A).

More severe than *Ppil1*$^{fs/fs}$, *Prp17* homozygous frameshift mice were lethal prior to E9.5 (c.277_287del11, E9.5, 0 mutant in 47 embryos, $p < 0.00001$, Binomial test). We further examined RNA splicing and cell survival in HEK293T cells after CRISPRi induced repression of PRP17 followed by expression of rescue PRP17 cDNAs (Gilbert et al., 2013). Both *Atg4d* and *Evi5l* minigene reporters showed higher intron retention levels after *PRP17* knockdown, rescued by WT but not p.F502C *PRP17* (Figures 6H, 6I, S7B, and S7C). We also observed that cell viability was significantly decreased after *PRP17* repression, which was almost fully rescued by WT but only slightly by p.F502C cDNA (Figure 6J). These results suggest that p.F502C impairs PRP17's function within the MSC in a fashion similar to PPIL1 patient variants.

PPIL1 mediated proline isomerization of PRP17 is not required for function

Given PPIL1 and PRP17 are both essential for embryonic development, and form an active PPIase-substrate pair, we hypothesized that catalyzed isomerization of PRP17 Gly94-Pro95 by PPIL1 is required for function. First, to rule out an effect of PPIL1 outside the spliceosome in the brain, we knocked in PPIL1 p.R131Q in mouse, since our results showed that this substitution selectively prevents its binding to SKIP, which recruits PPIL1 to the spliceosome (Wang et al., 2010). Homozygous *Ppil1*$^{R131Q/R131Q}$ mice showed perinatal lethality, microcephaly, and evidence of neurodegeneration in a fashion similar to *Ppil1*$^{A99T/A99T}$ (Figures 6K–6N and S7D–S7F). Selected splicing defects identified in *Ppil1*$^{A99T/A99T}$ brains were also confirmed in *Ppil1*$^{R131Q/R131Q}$ brains (Figures 6O and 6P). Although we obsered a slightly reduced PPIL1 protein (~ 30%) in *Ppil1*$^{R131Q/R131Q}$ embyros (Figures S7D and S7E), this is not sufficient to cause PCHM since heterozygous *Ppil1*$^{A99T/+}$ showed even a higher reduction (~ 40%) but did not show any phenotype (Figures S2F and S2G). Together, we conclude that PPIL1 mediates its effect in the brain by subserving its role in the spliceosome.

Second, we generated two additional knockin mouse lines: isomerase-inactive PPIL1 p.Arg55Ala (Davis et al., 2010; Zhang et al., 2013; Zydowsky et al., 1992), and non-isomerizable PRP17 p.Pro95Ala. We reasoned that if isomerization catalysis is crucial, these mutations should phenocopy patient mutations. Surprisingly, we observed no phenotype in either homozygous mutant: both *Ppil1*$^{R55A/R55A}$ and *Prp17*$^{P95A/P95A}$ were viable, fertile, and showed no microcephaly, cell death, or defective cortical lamination (Figures 6K–6N). Likewise, splicing defects were not observed in *Ppil1*$^{R55A/R55A}$ or *Prp17*$^{P95A/P95A}$ mice (Figures 6O and 6P). To confirm these results *in vitro*, we performed rescue assays in cultured cells by re-expressing either p.R55A PPIL1 or p.P95A PRP17. We found both mutants rescued proliferation and splicing defects as well as WT (Figures 6H–6J and S7G-S7J). Thus, while PPIL1 is capable of catalyzing PRP17 isomerization, and both are required for RNA splicing and mutated in human brain disease, their enzymatic interaction is not an essential part of the function of either protein. This data suggests the two proteins maintain a scaffolding rather than an enzyme-substrate interaction.

DISCUSSION

Here, we report that biallelic, partial loss-of-function mutations in *PPIL1* and *PRP17*, encoding two core spliceosomal components, disrupt RNA splicing integrity and lead to neurodegenerative pontocerebellar hypoplasia with microcephaly in human and mouse. The reported patients showed severe congenital microcephaly and simplified cortical gyri, which are rarely observed in other reported PCH types. We described this unique form of PCH as a new clinical entity PCHM, wherein spliceosome genes are the major contributors. Thus, our study highlighted the essential role of global splicing integrity in brain development and neurodegeneration, and uncovered a new pathway and mechanism underlying this heterogeneous group of degenerative brain disorders.

In general, clinical severity correlated with degree of impairment of protein stability or function by different patient variants, although T107A only reduced SKIP binding moderately, yet the affected children were severely affected, suggesting a potential unexplored mechanism or possible environmental contributions.

PPIL1 and PRP17 form an active enzyme-substrate pair in the spliceosome, and both are required for RNA splicing and neuronal survival. Surprisingly, our results showed PPIL1-mediated isomerization of PRP17 was not critical for their functions in splicing and neuronal survival, thus revealing a predominant non-enzymatic function of a spliceosome isomerase. Previous *in vitro* work also suggested that the enzymatic activity of PPIL1 is not required for splicing of selective pre-mRNA substrates (Adams et al., 2015). In line with this, only trans PRP17 G94-P95 was observed in MSC structures reported to date (Figures S7K and S7L). In the spliceosome, PPIL1 interacts with PRP17, RBM22, and SKIP. RBM22 is an RNA interacting protein, grasping the 5' intron right after the 5'SS region where U6 snRNA hybridizes (Bertram et al., 2017; Haselbach et al., 2018; Zhan et al., 2018a; Zhang et al., 2017), whereas the PRP17 WD40 domain binds to the intron branching point/U2 duplex (Movie S1). Both N-terminal SKIP and PRP17 are intrinsically disordered and undergo disorder-order transition upon PPIL1 binding (Wang et al., 2010; Zhang et al., 2017; Zhang et al., 2018). We propose that PPIL1 stabilizes these structures, allowing the MSC to function as a 'torque wrench' to bend 'challenged' introns to bring the 5'SS and the branching point into proximity. Loss of PPIL1 may reduce the ability to 'torque' the more rigid introns, which would explain the primary impacts on short and high GC content introns.

Although mutations in MSC genes had been linked to several types of diseases such as cancer and autosomal-dominant retinitis pigmentosa (Nik and Bowman, 2019; Scotti and Swanson, 2016; Singh and Cooper, 2012), our study is, to our knowledge, the first to connect MSC gene mutations and global splicing integrity to neuronal survival and neurodegeneration.

Why do mutations in these ubiquitously expressed spliceosomal genes lead to brain-specific disease? In our mouse model, apoptosis was limited to postmitotic neurons in homozygous KI mice, strikingly different from other microcephaly models which affect mitosis and survival of neural progenitors or show premature neurogenesis (Gruber et al., 2011; Insolera et al., 2014; Silver et al., 2010). Moreover, defects were observed across the body of compound heterozygous *Ppil1*$^{A99T/fs}$ mice. These suggest a distinct mechanism in PCHM and also reveals a higher susceptibility of neurons to global splicing perturbation. The developing brain expresses longer genes with more AS (Lipscombe

and Lopez Soto, 2019; Raj and Blencowe, 2015; Yeo and Burge, 2004), which might render neurons more susceptible. Postmitotic neurons might accumulate higher levels of misspliced mRNA, impacting protein production or accumulating toxic or unfolded proteins. Loss of *PPIL1* predominantly impacted AS of brain-expressed or brain-disease genes, involved in protein translation, DNA repair, and noncoding RNA processing, whose disruptions are the main causes for degeneration in cerebellar ataxia. Moreover, we further found evidence for DNA double-strand breaks with upregulated p53 and CC3 expression, consistent with accumulated transcriptional R-loops (Costantino and Koshland, 2018), although the exact mechanism remains to be explored. All these suggest a potentially shared mechanism of neurodegeneration underlying several genetic forms of PCH.

ACKNOWLEDGMENTS

This work was supported by SFARI 51486313, NIH R01NS048453, R01NS09800, QNRF NPRP 6-1463-3-351 (to J.G.G.), UM1HG008900/Broad Institute Center for Mendelian Genomics U54HG006504/Yale Center for Mendelian Disorders, N01 268201700006I-0-26800029 to CIDR for genotyping. J.G.G. is an investigator with the Howard Hughes Medical Institute, and received support from Rady Children's Institute for Genomic Medicine. We thank Peter Jackson (Stanford) for mass spectrometry analysis, Xiang-Dong Fu, Susan Taylor, Joshua Mayfield, and Jack Dixon for comments, UCSD Mouse Transgenic Core, UCSD CTRI (UL1TR001442) for biostatistics support, UCSD Neuroscience Core (P30 NS047101) and UCSD IGM Genomics Core.

AUTHOR CONTRIBUTIONS

GC, AW, ES, and JGG conceived the project and wrote the manuscript with input from all coauthors. CL, DA, SL, XY provided computational support, VS, PA, MWB supported mouse work, PG, KJW, BH-Y C, M H-Y T, LSP, AKL, GEVN, HLR, RM, EL, JD, AN, DP, EMAV, DTB, CJ, MSA, SA, MYI, and MZ recruited patients, LK, AK, IM PJ performed NMR.

REFERENCES

Adams, B.M., Coates, M.N., Jackson, S.R., Jurica, M.S., and Davis, T.L. (2015). Nuclear cyclophilins affect spliceosome assembly and function in vitro. Biochem J *469*, 223-233.

Agafonov, D.E., Deckert, J., Wolf, E., Odenwalder, P., Bessonov, S., Will, C.L., Urlaub, H., and Luhrmann, R. (2011). Semiquantitative proteomic analysis of the human spliceosome via a novel two-dimensional gel electrophoresis method. Mol Cell Biol *31*, 2667-2682.

Akizu, N., Cantagrel, V., Schroth, J., Cai, N., Vaux, K., McCloskey, D., Naviaux, R.K., Van Vleet, J., Fenstermaker, A.G., Silhavy, J.L.*, et al.* (2013). AMPD2 regulates GTP synthesis and is mutated in a potentially treatable neurodegenerative brainstem disorder. Cell *154*, 505-517.

Bertram, K., Agafonov, D.E., Liu, W.T., Dybkov, O., Will, C.L., Hartmuth, K., Urlaub, H., Kastner, B., Stark, H., and Luhrmann, R. (2017). Cryo-EM structure of a human spliceosome activated for step 2 of splicing. Nature *542*, 318-323.

Bessonov, S., Anokhina, M., Krasauskas, A., Golas, M.M., Sander, B., Will, C.L., Urlaub, H., Stark, H., and Luhrmann, R. (2010). Characterization of purified human Bact spliceosomal complexes reveals compositional and morphological changes during spliceosome activation and first step catalysis. RNA *16*, 2384-2403.

Breuss, M.W., Sultan, T., James, K.N., Rosti, R.O., Scott, E., Musaev, D., Furia, B., Reis, A., Sticht, H., Al-Owain, M.*, et al.* (2016). Autosomal-recessive mutations in the tRNA splicing endonuclease subunit TSEN15 cause pontocerebellar hypoplasia and progressive microcephaly. Am J Hum Genet *99*, 228-235.

Budde, B.S., Namavar, Y., Barth, P.G., Poll-The, B.T., Nurnberg, G., Becker, C., van Ruissen, F., Weterman, M.A., Fluiter, K., te Beek, E.T.*, et al.* (2008). tRNA splicing endonuclease mutations cause pontocerebellar hypoplasia. Nat Genet *40*, 1113-1118.

Cassandrini, D., Biancheri, R., Tessa, A., Di Rocco, M., Di Capua, M., Bruno, C., Denora, P.S., Sartori, S., Rossi, A., Nozza, P.*, et al.* (2010). Pontocerebellar hypoplasia: clinical, pathologic, and genetic studies. Neurology *75*, 1459-1464.

Chabot, B., and Shkreta, L. (2016). Defective control of pre-messenger RNA splicing in human disease. J Cell Biol *212*, 13-27.

Costantino, L., and Koshland, D. (2018). Genome-wide map of R-Loop-Induced damage reveals how a subset of R-Loops contributes to genomic instability. Mol Cell *71*, 487-497 e483.

Crooks, G.E., Hon, G., Chandonia, J.M., and Brenner, S.E. (2004). WebLogo: a sequence logo generator. Genome Res *14*, 1188-1190.

Davis, T.L., Walker, J.R., Campagna-Slater, V., Finerty Jr, P.J., Paramanathan, R., Bernstein, G., MacKenzie, F., Tempel, W., Ouyang, H., and Lee, W.H. (2010). Structural and biochemical characterization of the human cyclophilin family of peptidyl-prolyl isomerases. PLoS biology *8*, e1000439.

Denis, M.M., Tolley, N.D., Bunting, M., Schwertz, H., Jiang, H., Lindemann, S., Yost, C.C., Rubner, F.J., Albertine, K.H., Swoboda, K.J.*, et al.* (2005). Escaping the nuclear confines: signal-dependent pre-mRNA splicing in anucleate platelets. Cell *122*, 379-391.

Dobin, A., Davis, C.A., Schlesinger, F., Drenkow, J., Zaleski, C., Jha, S., Batut, P., Chaisson, M., and Gingeras, T.R. (2013). STAR: ultrafast universal RNA-seq aligner. Bioinformatics *29*, 15-21.

Dujardin, M., Madan, V., Montserret, R., Ahuja, P., Huvent, I., Launay, H., Leroy, A., Bartenschlager, R., Penin, F., Lippens, G.*, et al.* (2015). A proline-tryptophan turn in the intrinsically disordered domain 2 of NS5A protein is essential for Hepatitis C virus RNA replication. J Biol Chem *290*, 19104-19120.

Evans, P.A., Dobson, C.M., Kautz, R.A., Hatfull, G., and Fox, R.O. (1987). Proline isomerism in staphylococcal nuclease characterized by NMR and site-directed mutagenesis. Nature *329*, 266-268.

Fica, S.M., Oubridge, C., Wilkinson, M.E., Newman, A.J., and Nagai, K. (2019). A human postcatalytic spliceosome structure reveals essential roles of metazoan factors for exon ligation. Science *363*, 710-714.

Gilbert, L.A., Larson, M.H., Morsut, L., Liu, Z., Brar, G.A., Torres, S.E., Stern-Ginossar, N., Brandman, O., Whitehead, E.H., Doudna, J.A.*, et al.* (2013). CRISPR-mediated modular RNA-guided regulation of transcription in eukaryotes. Cell *154*, 442-451.

Gruber, R., Zhou, Z., Sukchev, M., Joerss, T., Frappart, P.O., and Wang, Z.Q. (2011). MCPH1 regulates the neuroprogenitor division mode by coupling the centrosomal cycle with mitotic entry through the Chk1-Cdc25 pathway. Nat Cell Biol *13*, 1325-1334.

Haselbach, D., Komarov, I., Agafonov, D.E., Hartmuth, K., Graf, B., Dybkov, O., Urlaub, H., Kastner, B., Luhrmann, R., and Stark, H. (2018). Structure and conformational dynamics of the human spliceosomal B(act) complex. Cell *172*, 454-464 e411.

Hewitt, S.H., Filby, M.H., Hayes, E., Kuhn, L.T., Kalverda, A.P., Webb, M.E., and Wilson, A.J. (2017). Protein surface mimetics: understanding how ruthenium tris(Bipyridines) interact with proteins. Chembiochem *18*, 223-231.

Insolera, R., Bazzi, H., Shao, W., Anderson, K.V., and Shi, S.H. (2014). Cortical neurogenesis in the absence of centrioles. Nat Neurosci *17*, 1528-1535.

Jangi, M., Fleet, C., Cullen, P., Gupta, S.V., Mekhoubad, S., Chiao, E., Allaire, N., Bennett, C.F., Rigo, F., Krainer, A.R.*, et al.* (2017). SMN deficiency in severe models of spinal muscular atrophy causes widespread intron retention and DNA damage. Proc Natl Acad Sci U S A *114*, E2347-E2356.

Joseph, J.T., Innes, A.M., Smith, A.C., Vanstone, M.R., Schwartzentruber, J.A., Bulman, D.E., Majewski, J., Daza, R.A., Hevner, R.F., Michaud, J.*, et al.* (2014). Neuropathologic features of pontocerebellar hypoplasia type 6. J Neuropathol Exp Neurol *73*, 1009-1025.

Karaca, E., Weitzer, S., Pehlivan, D., Shiraishi, H., Gogakos, T., Hanada, T., Jhangiani, S.N., Wiszniewski, W., Withers, M., Campbell, I.M.*, et al.* (2014). Human CLP1 mutations alter tRNA biogenesis, affecting both peripheral and central nervous system function. Cell *157*, 636-650.

Kishore, S., Khanna, A., and Stamm, S. (2008). Rapid generation of splicing reporters with pSpliceExpress. Gene *427*, 104-110.

Kolde, R., and Kolde, M.R. (2015). Package 'pheatmap'. R Package *1*.

Lee, S., Chen, D.Y., Zaki, M.S., Maroofian, R., Houlden, H., Di Donato, N., Abdin, D., Morsy, H., Mirzaa, G.M., Dobyns, W.B.*, et al.* (2019). Bi-allelic Loss of Human APC2, Encoding Adenomatous Polyposis Coli Protein 2, Leads to Lissencephaly, Subcortical Heterotopia, and Global Developmental Delay. Am J Hum Genet *105*, 844-853.

Li, Y.I., Knowles, D.A., Humphrey, J., Barbeira, A.N., Dickinson, S.P., Im, H.K., and Pritchard, J.K. (2018). Annotation-free quantification of RNA splicing using LeafCutter. Nat Genet *50*, 151-158.

Lines, M.A., Huang, L., Schwartzentruber, J., Douglas, S.L., Lynch, D.C., Beaulieu, C., Guion-Almeida, M.L., Zechi-Ceide, R.M., Gener, B., Gillessen-Kaesbach, G.*, et al.* (2012). Haploinsufficiency of a spliceosomal GTPase encoded by EFTUD2 causes mandibulofacial dysostosis with microcephaly. Am J Hum Genet *90*, 369-377.

Lipscombe, D., and Lopez Soto, E.J. (2019). Alternative splicing of neuronal genes: new mechanisms and new therapies. Curr Opin Neurobiol *57*, 26-31.

Martin, M. (2011). Cutadapt removes adapter sequences from high-throughput sequencing reads. EMBnet journal *17*, 10-12.

Namavar, Y., Barth, P.G., Kasher, P.R., van Ruissen, F., Brockmann, K., Bernert, G., Writzl, K., Ventura, K., Cheng, E.Y., Ferriero, D.M.*, et al.* (2011). Clinical, neuroradiological and genetic findings in pontocerebellar hypoplasia. Brain *134*, 143-156.

Nik, S., and Bowman, T.V. (2019). Splicing and neurodegeneration: Insights and mechanisms. Wiley Interdiscip Rev RNA *10*, e1532.

Paulsen, R.D., Soni, D.V., Wollman, R., Hahn, A.T., Yee, M.C., Guan, A., Hesley, J.A., Miller, S.C., Cromwell, E.F., Solow-Cordero, D.E., *et al.* (2009). A genome-wide siRNA screen reveals diverse cellular processes and pathways that mediate genome stability. Mol Cell *35*, 228-239.
Pellagatti, A., and Boultwood, J. (2017). Splicing factor gene mutations in the myelodysplastic syndromes: impact on disease phenotype and therapeutic applications. Adv Biol Regul *63*, 59-70.
Quinlan, A.R., and Hall, I.M. (2010). BEDTools: a flexible suite of utilities for comparing genomic features. Bioinformatics *26*, 841-842.
Raj, B., and Blencowe, B.J. (2015). Alternative splicing in the mammalian nervous system: recent insights into mechanisms and functional roles. Neuron *87*, 14-27.
Rajiv, C., and Davis, T.L. (2018). Structural and functional insights into human nuclear cyclophilins. Biomolecules *8*, 161.
Ran, F.A., Hsu, P.D., Wright, J., Agarwala, V., Scott, D.A., and Zhang, F. (2013). Genome engineering using the CRISPR-Cas9 system. Nat Protoc *8*, 2281-2308.
Rappsilber, J., Ryder, U., Lamond, A.I., and Mann, M. (2002). Large-scale proteomic analysis of the human spliceosome. Genome Res *12*, 1231-1245.
Ruzickova, S., and Stanek, D. (2017). Mutations in spliceosomal proteins and retina degeneration. RNA Biol *14*, 544-552.
Schaffer, A.E., Eggens, V.R., Caglayan, A.O., Reuter, M.S., Scott, E., Coufal, N.G., Silhavy, J.L., Xue, Y., Kayserili, H., Yasuno, K., *et al.* (2014). CLP1 founder mutation links tRNA splicing and maturation to cerebellar development and neurodegeneration. Cell *157*, 651-663.
Schwarz, J.M., Cooper, D.N., Schuelke, M., and Seelow, D. (2014). MutationTaster2: mutation prediction for the deep-sequencing age. Nat Methods *11*, 361-362.
Scotti, M.M., and Swanson, M.S. (2016). RNA mis-splicing in disease. Nat Rev Genet *17*, 19-32.
Shen, S., Park, J.W., Lu, Z.X., Lin, L., Henry, M.D., Wu, Y.N., Zhou, Q., and Xing, Y. (2014). rMATS: robust and flexible detection of differential alternative splicing from replicate RNA-Seq data. Proc Natl Acad Sci U S A *111*, E5593-5601.
Shen, Y., and Bax, A. (2010). Prediction of Xaa-Pro peptide bond conformation from sequence and chemical shifts. J Biomol NMR *46*, 199-204.
Shi, Y. (2017). Mechanistic insights into precursor messenger RNA splicing by the spliceosome. Nat Rev Mol Cell Biol *18*, 655-670.
Silver, D.L., Watkins-Chow, D.E., Schreck, K.C., Pierfelice, T.J., Larson, D.M., Burnetti, A.J., Liaw, H.J., Myung, K., Walsh, C.A., Gaiano, N., *et al.* (2010). The exon junction complex component Magoh controls brain size by regulating neural stem cell division. Nat Neurosci *13*, 551-558.
Singh, R.K., and Cooper, T.A. (2012). Pre-mRNA splicing in disease and therapeutics. Trends Mol Med *18*, 472-482.
Sobreira, N., Schiettecatte, F., Valle, D., and Hamosh, A. (2015). GeneMatcher: a matching tool for connecting investigators with an interest in the same gene. Hum Mutat *36*, 928-930.
Sorrells, S., Nik, S., Casey, M., Cameron, R.C., Truong, H., Toruno, C., Gulfo, M., Lowe, A., Jette, C., Stewart, R.A., *et al.* (2018). Spliceosomal components protect embryonic neurons from R-loop-mediated DNA damage and apoptosis. Dis Model Mech *11*.
Stegmann, C.M., Luhrmann, R., and Wahl, M.C. (2010). The crystal structure of PPIL1 bound to cyclosporine A suggests a binding mode for a linear epitope of the SKIP protein. PLoS One *5*, e10013.
Synofzik, M., Puccio, H., Mochel, F., and Schols, L. (2019). Autosomal recessive cerebellar ataxias: paving the way toward targeted molecular therapies. Neuron *101*, 560-583.
Teigelkamp, S., Achsel, T., Mundt, C., Gothel, S.F., Cronshagen, U., Lane, W.S., Marahiel, M., and Luhrmann, R. (1998). The 20kD protein of human [U4/U6.U5] tri-snRNPs is a novel

cyclophilin that forms a complex with the U4/U6-specific 60kD and 90kD proteins. RNA *4*, 127-141.
Turnbull, W.B., and Daranas, A.H. (2003). On the value of c: can low affinity systems be studied by isothermal titration calorimetry? J Am Chem Soc *125*, 14859-14866.
van Dijk, T., Baas, F., Barth, P.G., and Poll-The, B.T. (2018). What's new in pontocerebellar hypoplasia? An update on genes and subtypes. Orphanet J Rare Dis *13*, 92.
Vangipuram, M., Ting, D., Kim, S., Diaz, R., and Schule, B. (2013). Skin punch biopsy explant culture for derivation of primary human fibroblasts. J Vis Exp, e3779.
Wang, X., Zhang, S., Zhang, J., Huang, X., Xu, C., Wang, W., Liu, Z., Wu, J., and Shi, Y. (2010). A large intrinsically disordered region in SKIP and its disorder-order transition induced by PPIL1 binding revealed by NMR. J Biol Chem *285*, 4951-4963.
Wickham, H. (2016). ggplot2: elegant graphics for data analysis (Springer).
Will, C.L., and Luhrmann, R. (2011). Spliceosome structure and function. Cold Spring Harb Perspect Biol *3*, a003707.
Xie, C., Mao, X., Huang, J., Ding, Y., Wu, J., Dong, S., Kong, L., Gao, G., Li, C.Y., and Wei, L. (2011). KOBAS 2.0: a web server for annotation and identification of enriched pathways and diseases. Nucleic Acids Res *39*, W316-322.
Xu, C., Xu, Y., Tang, Y., Wu, J., Shi, Y., Huang, Q., and Zhang, Q. (2005). Backbone and side chain assignments of human Peptidylprolyl Isomerase Like 1 (hPPIL1). J Biomol NMR *31*, 179-180.
Xu, C., Zhang, J., Huang, X., Sun, J., Xu, Y., Tang, Y., Wu, J., Shi, Y., Huang, Q., and Zhang, Q. (2006). Solution structure of human peptidyl prolyl isomerase-like protein 1 and insights into its interaction with SKIP. J Biol Chem *281*, 15900-15908.
Xu, M., Xie, Y.A., Abouzeid, H., Gordon, C.T., Fiorentino, A., Sun, Z., Lehman, A., Osman, I.S., Dharmat, R., Riveiro-Alvarez, R.*, et al.* (2017). Mutations in the Spliceosome Component CWC27 Cause Retinal Degeneration with or without Additional Developmental Anomalies. Am J Hum Genet *100*, 592-604.
Yan, C., Hang, J., Wan, R., Huang, M., Wong, C.C., and Shi, Y. (2015a). Structure of a yeast spliceosome at 3.6-angstrom resolution. Science *349*, 1182-1191.
Yan, Q., Weyn-Vanhentenryck, S.M., Wu, J., Sloan, S.A., Zhang, Y., Chen, K., Wu, J.Q., Barres, B.A., and Zhang, C. (2015b). Systematic discovery of regulated and conserved alternative exons in the mammalian brain reveals NMD modulating chromatin regulators. Proc Natl Acad Sci U S A *112*, 3445-3450.
Yeo, G., and Burge, C.B. (2004). Maximum entropy modeling of short sequence motifs with applications to RNA splicing signals. J Comput Biol *11*, 377-394.
Zhan, X., Yan, C., Zhang, X., Lei, J., and Shi, Y. (2018a). Structure of a human catalytic step I spliceosome. Science *359*, 537-545.
Zhan, X., Yan, C., Zhang, X., Lei, J., and Shi, Y. (2018b). Structures of the human pre-catalytic spliceosome and its precursor spliceosome. Cell Res *28*, 1129-1140.
Zhang, X., Chen, M.H., Wu, X., Kodani, A., Fan, J., Doan, R., Ozawa, M., Ma, J., Yoshida, N., Reiter, J.F.*, et al.* (2016). Cell-type-specific alternative splicing governs cell fate in the developing cerebral cortex. Cell *166*, 1147-1162 e1115.
Zhang, X., Yan, C., Hang, J., Finci, L.I., Lei, J., and Shi, Y. (2017). An atomic structure of the human spliceosome. Cell *169*, 918-929 e914.
Zhang, X., Yan, C., Zhan, X., Li, L., Lei, J., and Shi, Y. (2018). Structure of the human activated spliceosome in three conformational states. Cell Res *28*, 307-322.
Zhang, X., Zhan, X., Yan, C., Zhang, W., Liu, D., Lei, J., and Shi, Y. (2019). Structures of the human spliceosomes before and after release of the ligated exon. Cell Res *29*, 274-285.
Zhang, X.C., Wang, W.D., Wang, J.S., and Pan, J.C. (2013). PPIase independent chaperone-like function of recombinant human Cyclophilin A during arginine kinase refolding. FEBS Lett *587*, 666-672.

Zhou, Y., Zhou, B., Pache, L., Chang, M., Khodabakhshi, A.H., Tanaseichuk, O., Benner, C., and Chanda, S.K. (2019). Metascape provides a biologist-oriented resource for the analysis of systems-level datasets. Nat Commun *10*, 1523.

Zhou, Z., Licklider, L.J., Gygi, S.P., and Reed, R. (2002). Comprehensive proteomic analysis of the human spliceosome. Nature *419*, 182-185.

Zydowsky, L.D., Etzkorn, F.A., Chang, H.Y., Ferguson, S.B., Stolz, L.A., Ho, S.I., and Walsh, C.T. (1992). Active site mutants of human cyclophilin A separate peptidyl-prolyl isomerase activity from cyclosporin A binding and calcineurin inhibition. Protein Sci *1*, 1092-1099.

Table 1. Clinical information of selected patients

Patient	Family 1-III:1	Family 3-III:1	Family 4-III:3	Family 5-III:1	Family 6-II:1	Family 7-II:1	Family 8-II:1	Family 9-II:1	Family 10-V:3
Mutation gRNA (hg19)	chr6:g.36823795C>T	chr6:g.36823771T>C	chr6:g.36824409T>C	chr6:g.36823698C>T	chr6:g.[36823772_36823789dup; 36823765C>A]	chr6:g.[36824397A>G];[36823698C>T]	chr6:g.[36823711T>C];[36824361C>T]	chr6:g.[36823711T>C];[36839572G>A]	PRP17 hg19:chr6:110550122T>G
Mutation cDNA PPIL1 NM_016059.1, PRP17 NM_015891.2	c.295G>A	c.319A>G	c.233A>G	c.392G>A	c.[301_318dup; 325G>T]	c.[245T>C]; [392G>A]	c.[379A>G]; [280+1G>A]	c.[379A>G];[133C>T]	PRP17 c.1505T>G
Mutation Protein PPIL1 NP_057143.1, PRP17 NP_056975.1	p.Ala99Thr	p.Thr107Ala	p.Tyr78Cys	p.Arg131Gln	p.[Ala101_Asp106dup;Gly109Cys]	p.[Phe82Ser; Arg131Gln]	p.[Thr127Ala];[?]	p.[Thr127Ala]; [Arg45*]	PRP17 p.Phe502Cys
Gender	Male	Male	Female	Female	Female	Male	Female	Male	Female
Ethnic origin	Egyptian	Pakistani	Mexican	Egyptian	Pakistani	Chinese	European-American	European-American	Egyptian
Parental consanguinity	+	+	+	+	+	-	-	-	+
Head circumference (HC) at birth	28cm (-6SD)	30cm (-4SD)	28cm (-4.5SD)	29cm (-4SD)	30cm (-4SD)	30cm (-2.5SD)	29cm (-4SD)	32cm (-2SD)	30cm (-3SD)
HC at last examination	36cm (-8SD) at 9 mos	39cm (-5SD) at 1 y	36cm (-8SD) at 9 mos	37cm (-6SD) at 9 mos	39cm (-5SD) at 1 y	45cm (-4SD) at 4 y	43cm (-8SD) at age 10 y	45.5cm (-6SD) at 13 y	42 cm (-5SD) at 4y
Pontocerebellar hypoplasia	+	+	+	+	+	+	+	+	+
Simplified cortical gyral patterning	+	+	+	+	+	-		-	-
Agenesis of corpus callosum	+	+	Partial	+	+	Partial		Partial	Partial
Cerebellar hypoplasia	+	+	+	+	+	+	+	+	+
Brainstem hypoplasia	+	+	+	+	+	+	+	+	+
Hydrocephalus	-	-	-	-	+	-		-	-
White matter abnormalities	-	-	Delayed myelination	-	-	-		Delayed myelination	-
Intellectual Disability	Severe	Severe	Severe	Severe	Severe	Severe	Severe	Severe	Severe
Seizure Onset	Birth	-	Infancy	Infancy	-	Infancy	Infancy	Infancy	Infancy
Seizure Type	Focal	-	Focal	Generalized	-	Myoclonic	Infantile spasms	Infantile spasms	Myoclonic / GTC
Seizure Frequency	Intractable	-	Infrequent	Infrequent	-	Monthly	Intractable	Daily, Intractable	Intractable
Gross motor	Absent	Absent	Absent	Delayed	Absent	Delayed	Absent	Absent	Delayed
Fine motor	Absent	Absent	Absent	Absent	Absent	Delayed	Absent	Absent	Absent
Language	Absent	Absent	Absent	Absent	Absent	Delayed	Absent	Absent	Absent
Social	Absent	Absent	Absent	Absent	Absent	Delayed	Absent	Absent	Absent
Hypertonia	Mild	-	-	Mild	-	-	Mild	Mild	Mild
Hypotonia	-	Severe	Severe	Mild	Severe	-	Mild	Mild	-

Deep tendon reflexes	Brisk	Brisk	Brisk	Brisk	Brisk	-	Brisk	Brisk	Brisk
Spastic tetraplegia	+	+	+	+	++	-	+	+	+
Other	Died at 8mos; Inguinal hernia	Died at 2mos; Persistent thrombocytopaenia	Dystonia; Chronic neutropenia		Died at 2 mos	Dystonia; Chronic neutropenia	Dystonia		Chronic anemia and thrombocytopenia

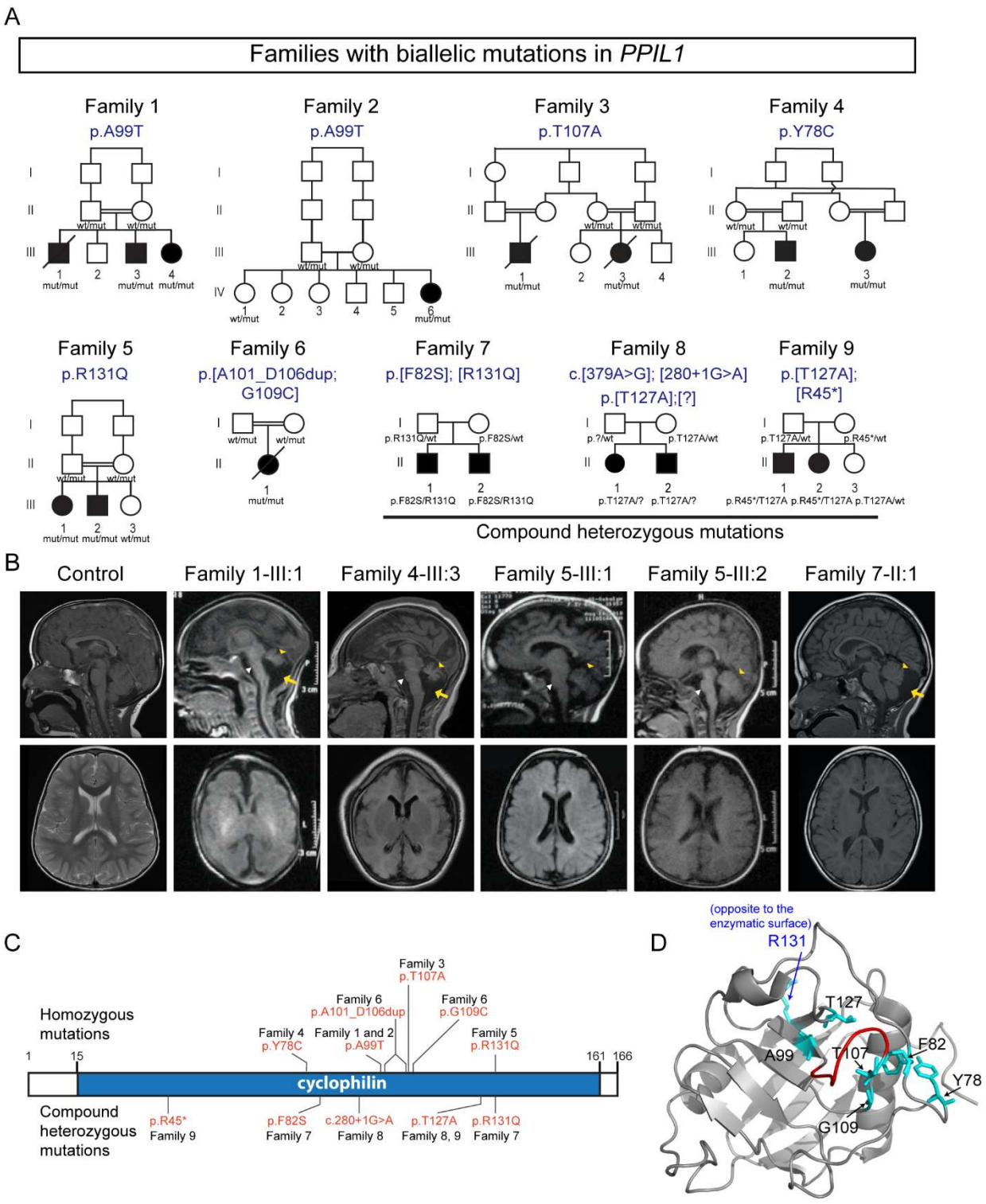

Figure 1. Biallelic mutations in *PPIL1* lead to neurodegenerative pontocerebellar hypoplasia with microcephaly (PCHM) in human

(A) The families with predicted effects of PPIL1 variants listed above pedigree. All variants are homozygous in affected individuals, except Family 7-9, which are compound

heterozygous. All pathogenic variants segregated as a recessive trait. Filled symbols: affected; p.[?]: splice donor site mutation, c.280+1G>A; square: male; circle: female; double bar: consanguinity; diagonal line: deceased. wt, reference allele; mut, patient variant allele.

(B) Sagittal (top) and axial (bottom) T1-weighted brain MRIs show reduced cerebellar volume (yellow arrowhead), atrophic pons (white arrowhead) and posterior fossa fluid accumulation (yellow arrows) indicative of cerebellar atrophy in affected individuals. Simplified gyri pattern is most apparent in the affected from Family 1 and 4.

(C) Identified *PPIL1* mutations. Above: homozygous variants. Below: compound heterozygous mutations.

(D) *En face* view of enzymatic surface with labeled variant residues in NMR-resolved PPIL1 structure (PDB: 2K7N). All except R131 (blue) localized to the enzymatic surface. Red: duplicated region in Family 6 (A101-D106).

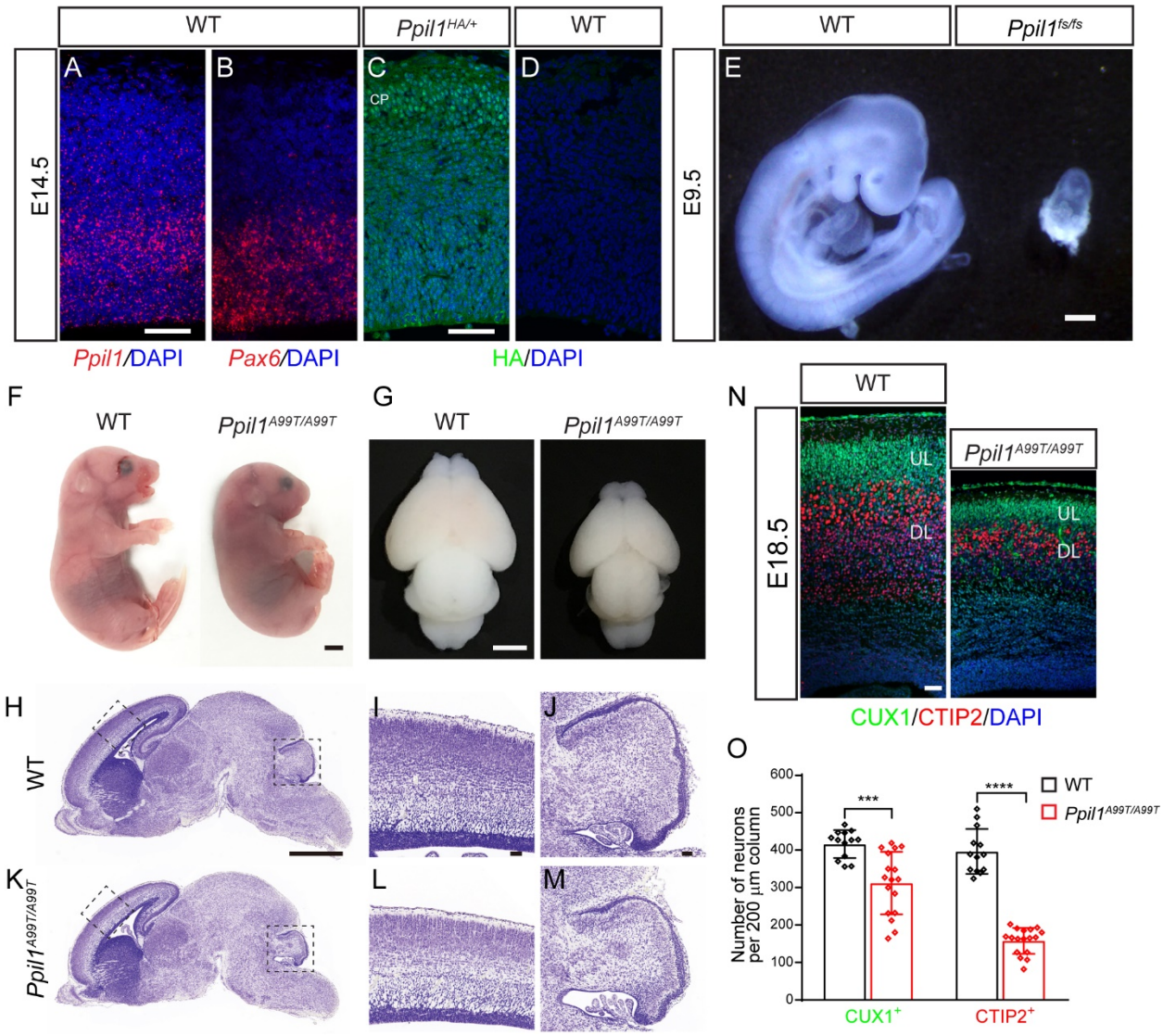

Figure 2. Patient *PPIL1* mutation knockin mice exhibit PCHM-like phenotype

(A and B) Fluorescent *in situ* hybridization (FISH) on coronal sections of E14.5 brain cortex hybridized with *Ppil1* (A) and *Pax6* (B) probes using RNAscope. Scale bar: 50 µm.

(C and D) Coronal sections of E14.5 embryos from *Ppil1*$^{HA/+}$ (C) and WT (D) embryos immunostained with an anti-HA antibody showing ubiquitous expression of PPIL1. CP: cortical plate. Bar: 50 µm.

(E) *Ppil1* $^{fs/fs}$ mouse embryos showed reabsorption at E9.5. Bar: 2 mm.

(F and G) Homozygous patient variant p.A99T knockin mouse with microcephaly at E18.5.

(H-M) Nissl stained sagittal sections of E18.5 *Ppil1*$^{A99T/A99T}$ brains, magnified for dashed regions in the cerebral cortex and cerebellum.

(N) E18.5 *Ppil1*$^{A99T/A99T}$ cortex (coronal) shows reduced thickness but with intact lamination based upon immunostaining against CUX1 (upper layer neurons) and CTIP2 (lower layer neurons).

(O) Reduced density of cortical CUX1^{+} and CTIP2^{+} neurons in E18.5 *Ppil1*$^{A99T/A99T}$ cortex. n = 4 mice/genotype. Unpaired t-test: $p = 0.0003$ CUX1^{+} cells; $p < 0.0001$ CTIP2^{+} cells. Scale bar: 1 mm in H and K; 50 μm in I, J, and L–M.

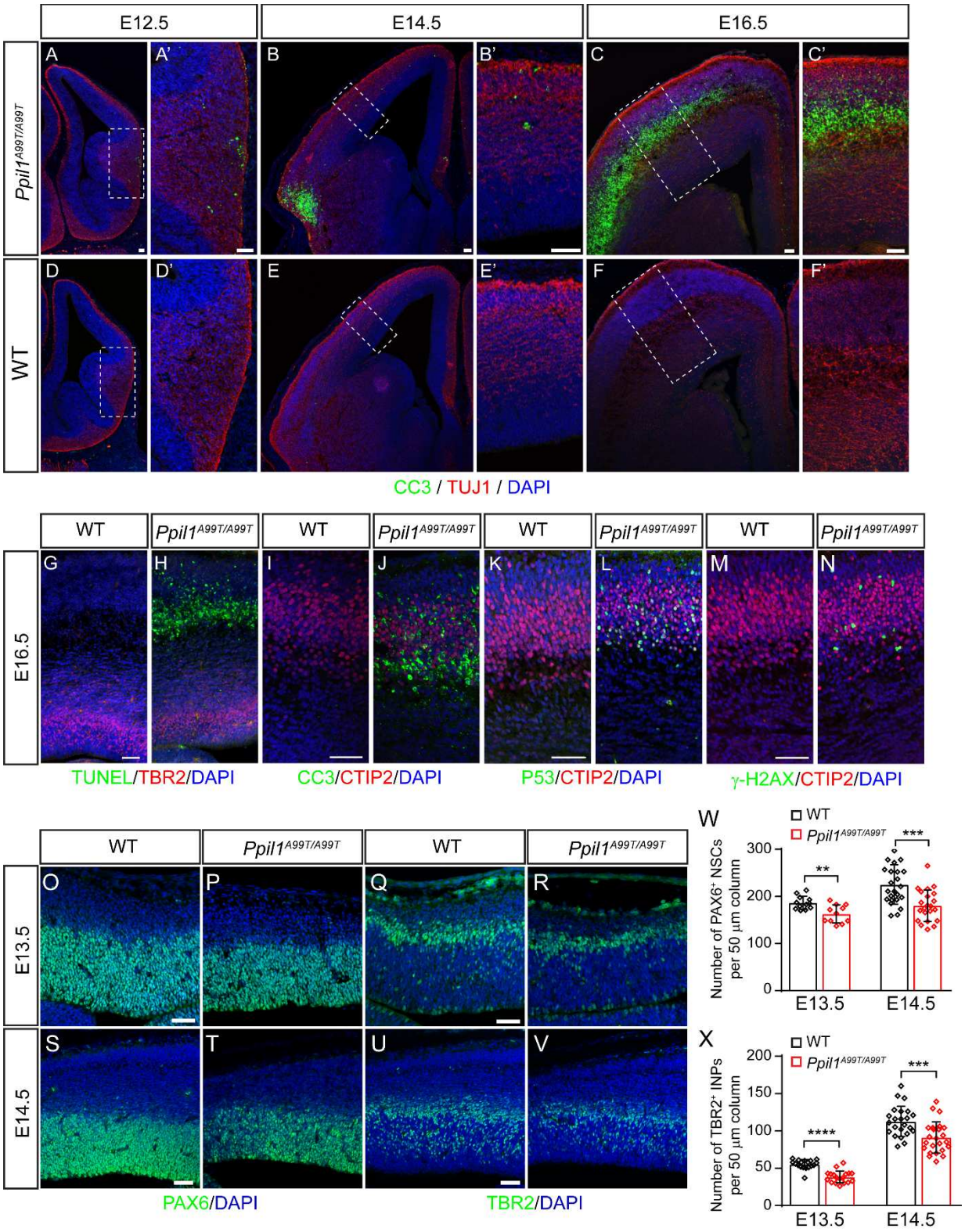

Figure 3. *Ppil1* knockin mice show increased neuron-specific apoptosis and depletion of neural progenitor cells

(A-F) Embryonic *Ppil1*$^{A99T/A99T}$ brains (coronal) shows increased cleaved Caspase 3 (CC3, green).
(G-N) Coronal sections of E16.5 brain cortex from WT and *Ppil1*$^{A99T/A99T}$ embryos stained for TUNEL and TBR2 (G and H), CC3 and CTIP2 (I and J), p53 and CTIP2 (K and L), γ-H2AX and CTIP2 (M and N).
(O-V) Embryonic *Ppil1*$^{A99T/A99T}$ cortex (coronal) shows reduced PAX6 (neural stem cells, NSC) and TBR2 (intermediate neural progenitor, INP) positive cells.
(W and X) Reduced density of cortical PAX6+ neural stem cells and TBR2+ intermediate progenitor cells in E13.5 and E14.5 cortex. Unpaired t-test: $p = 0.0029$ E13.5 PAX6+, $p = 0.0002$ E14.5 PAX6+; $p < 0.0001$ E13.5 TBR2+; $p = 0.0008$ E14.5 TBR2+.
Scale bar: 50 μm.

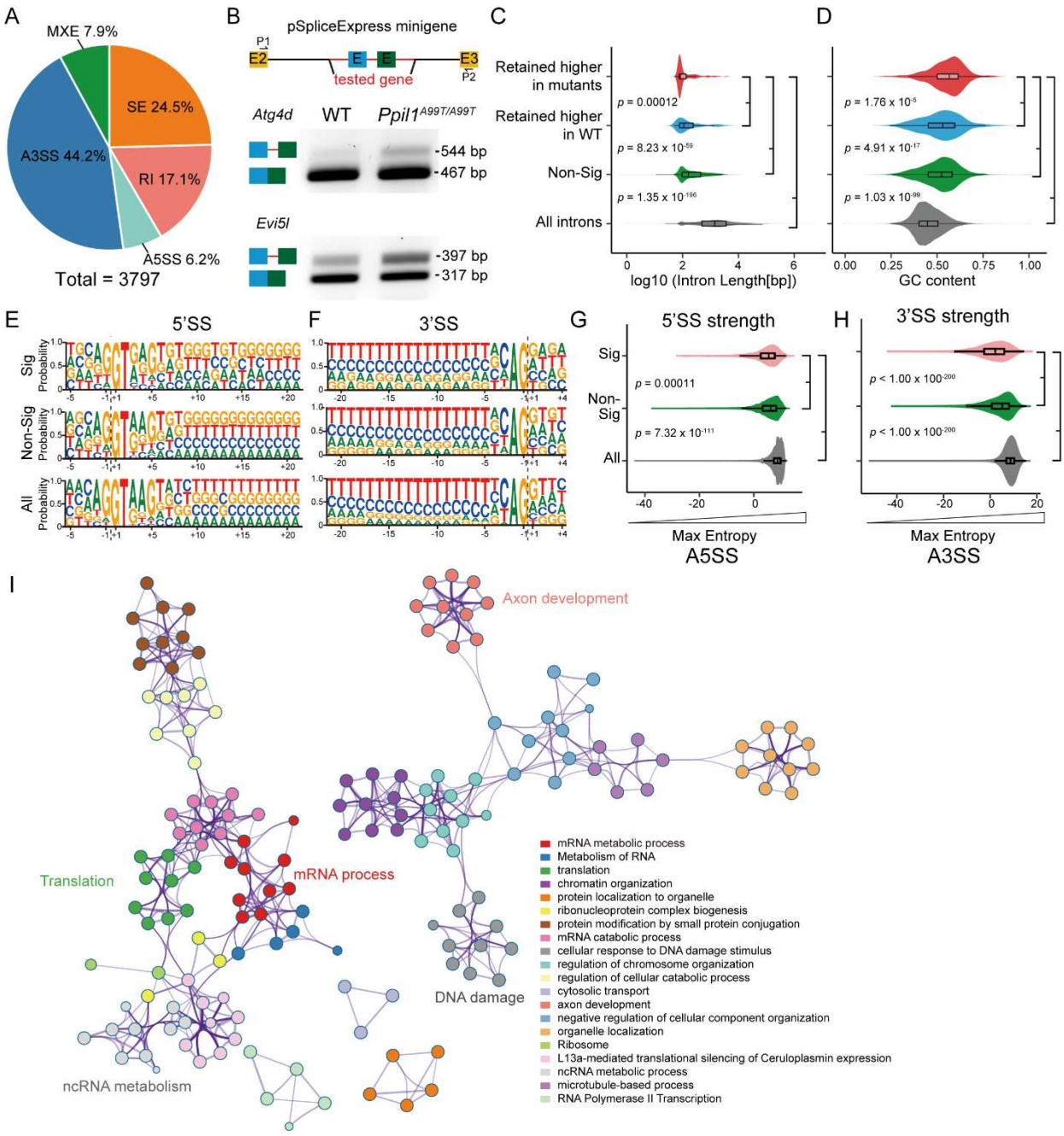

Figure 4. Global splicing integrity defects in *Ppil1*$^{A99T/A99T}$ developing brain

(A) Impact of p.A99T mutation on five major types of AS events detected with rMATS in E14.5 brain hemispheres (3 KI vs. 3WT). A3SS was most impacted, followed by SE, RI, MXE, and A5SS.

(B) Minigene splicing reporter assays in transfected *Ppil1*$^{A99T/A99T}$ mouse embryonic fibroblasts show higher intron retention levels in mutant cells for both *Atg4d* and *Evi5l*.

(C and D) Distribution of differential splicing in KI or control, based upon intron length and GC content. Introns with short length or high GC content show significantly retained higher in *Ppil1* KI brains. *p*-value: Wilcox test.

(E-H) Splice-site strength analysis of 5'SS and 3'SS in all introns (All, gray), non-significant A5SS or A3SS events (Non-sig, green), and significant A5SS or A3SS events (Sig, red) identified by rMATS. The 5'SS and 3'SS strength show lower maximum entropy for choice points that were significantly different in KI compared with control. *p*-value: Wilcox test.

(I) Metascape visualization of enriched networks and pathways among all misspliced genes in E14.5 *Ppil1*$^{A99T/A99T}$ brains (n = 2134 misspliced genes), showing several key modules represented including "mRNA metabolic process" among others.

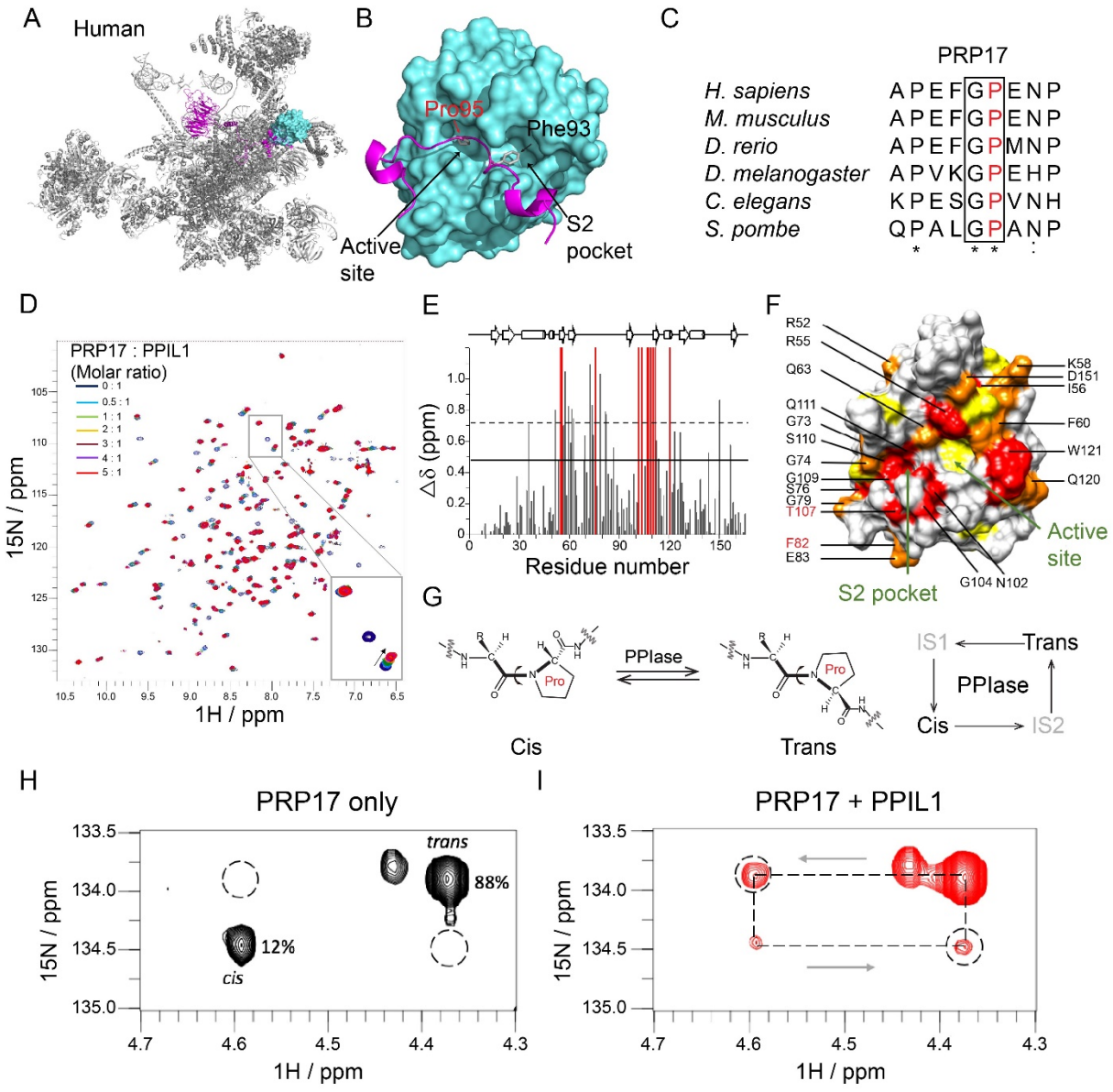

Figure 5. PPIL1 P95 is positioned in the enzymatic pocket of PRP17 in the activated spliceosome

(A and B) Cryo-EM structure of human spliceosome C* complex (PDB: 5XJC) shows an N-terminal loop of PRP17 (cartoon in purple) bound to PPIL1 (teal) enzymatic surface with Pro95 buried inside the S1 enzymatic pocket.

(C) Protein sequence alignment of PRP17 from 6 species shows an evolutionarily conserved Gly-Pro (G-P) motif in PRP17. * stands for identical residues, : indicates similar residues.

(D) Overlaid ^{1}H-^{15}N HSQC spectra of PPIL1 with PRP17 peptide titrations (0-5 molar equivalents, aa 89-101: FAPEFG[P]ENPFRT). Specific resonance shifts or broadening beyond detection indicates specific binding of PRP17 to PPIL1. Inset: Examples of PPIL1 resonance changes that shift (arrowhead), broaden beyond detection (open arrowhead) or were unchanged (arrow) as a result of PRP17 titration.

(E) Average chemical shift perturbations of PPIL1 residues upon titration with PRP17. Gray: shifted resonances. Red: broadened beyond detection resonances. Solid or dashed lines: shifts >1 or >2 SD above mean, respectively.

(F) Space-filling model of PPIL1 (PDB: 2X7K) showed significantly perturbed residues upon PRP17 peptide binding. Red: residues broadened beyond detection, Orange: residues >2 SD, Yellow: residues >1 SD above mean. Residues affected in patients are labeled in red.

(G) Schematic of cis-trans Xaa-Pro peptide bond isomerization catalyzed by PPIase. IS: Intermediate State.

(H and I) 2D ^{1}H, ^{15}N-H($C\alpha$)N ZZ exchange spectra of PRP17 peptide in the absence (H) or presence (I) of sub-stoichiometric concentrations (1% molar ratio) of PPIL1, with appearance of 'exchange signals' (dashed circles), i.e. significant interconversion between cis-trans states.

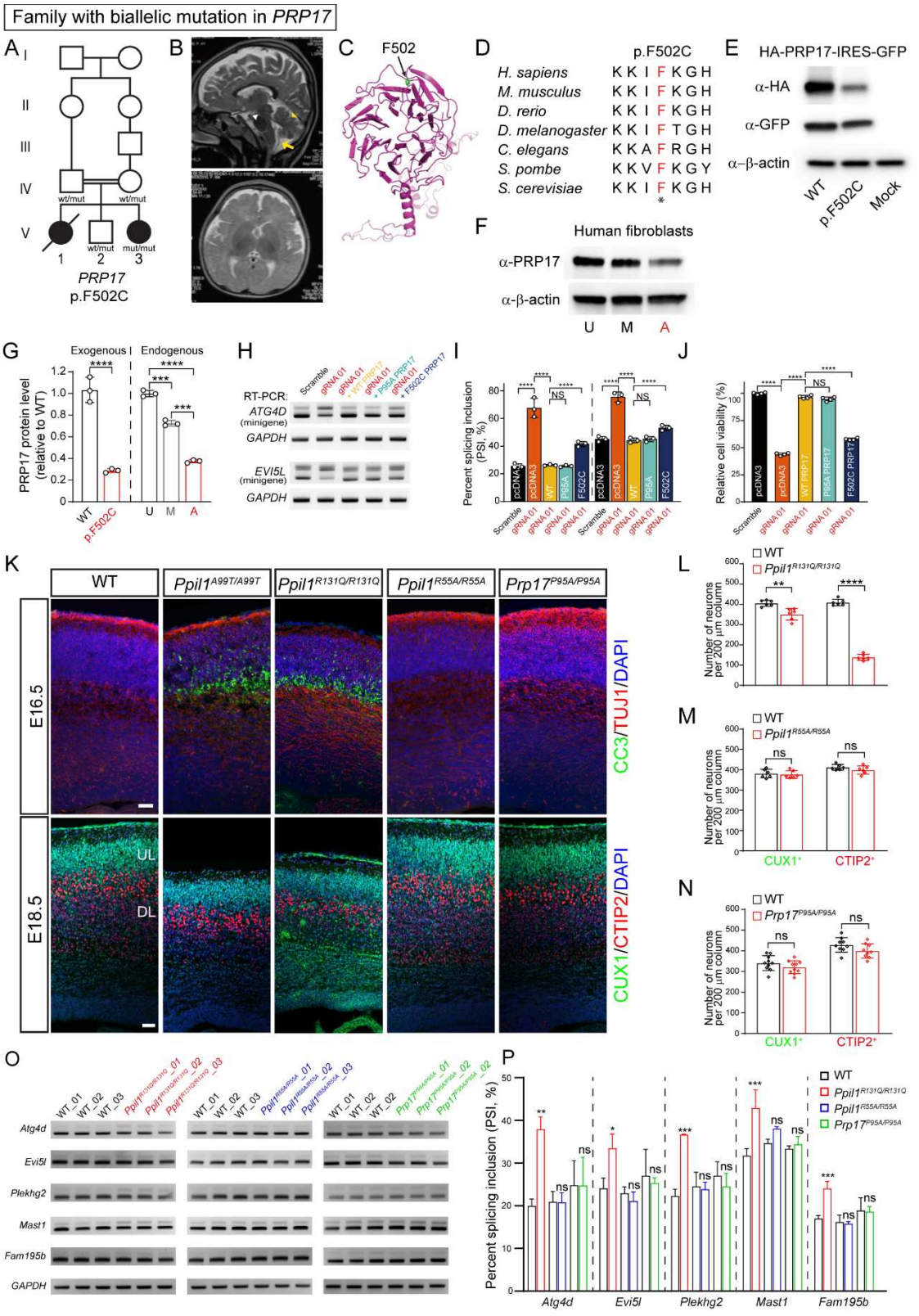

Figure 6. *PPIL1* and *PRP17* control neuronal survival independent of catalysis

(A) Pedigrees of PCHM Family 10 with homozygous *PRP17* p.F502C variant segregating as a recessive trait. Filled symbols: affected; square: male; circle: female; double bar: consanguinity; diagonal line: deceased.

(B) T2-weighted brain MRI shows reduced cerebellar volume (yellow arrowhead), atrophic pons (white arrowhead) and posterior fossa fluid accumulation (yellow arrows) indicative of cerebellar atrophy in the living affected.

(C) The structure of PRP17 resolved from the cryo-EM structure of spliceosomal C complex (PDB: 5XJC) showing mutated residue F502 within the C-terminal WD40 domain.

(D) Protein sequence alignment of *PRP17* showing mutated F502 residue highly conserved across eukaryotes. *: identical.

(E) Western blot of overexpressed HA-tagged PRP17 shows that the p.F502C substitution destabilized the protein.

(F) Western blot of endogenous PRP17 from dermal fibroblasts demonstrating reduced protein levels from affected (A) compared with mother (M) and unaffected control (U).

(G) Quantification of exogenous and endogenous PRP17 protein in transfected HEK293T cells and human dermal fibroblasts, respectively. n = 3.

(H) RT-PCR based minigene splicing assay following PRP17 repression in HEK293T cells, showing full rescue by WT or p.P95A PRP17 but only partial rescue by p.F502C PRP17.

(I) Quantification of percent splicing inclusion (PSI) for minigene splicing reporters. PSI was calculated as percent of inclusion form transcripts among all transcripts (inclusion and exclusion forms). n = 3.

(J) Reduced cell viability following *PRP17* repression was fully rescued by WT or p.P95A PRP17 but only partially by p.F502C PRP17. n = 4.

(K) Coronal sections of E16.5 (top) and E18.5 (bottom) mouse brains with upregulated cleaved caspase 3 (CC3) and reduced cortical thickness in $Ppil1^{A99T/A99T}$ and $Ppil1^{R131Q/R131Q}$, but not in $Ppil1^{R55A/R55A}$ or $Prp17^{P95A/P95A}$. CUX1 and CTIP2 label upper and deep layer cortical neurons, respectively. Scale bar: 50 μm.

(L–N) Quantification of cortical $CUX1^{+}$ and $CTIP2^{+}$ neurons in E18.5 cortex of $Ppil1^{R131Q/R131Q}$ (L), $Ppil1^{R55A/R55A}$ (M), $Prp17^{P95A/P95A}$ (N), and littermate controls. n = 3 mice/genotype.

(O) Semi-quantitative RT-PCR analysis of significant RI events in $Ppil1^{A99T/A99T}$ among E14.5 brains of $Ppil1^{R131Q/R131Q}$ (red), $Ppil1^{R55A/R55A}$ (blue), $Prp17^{P95A/P95A}$ (green), and littermate controls. *GAPDH* as loading control.

(P) Quantification of percent splicing inclusion (PSI) for RI events. n = 3 for each genotype.

Mean ± s.d. *p*-value: ns > 0.05; * <0.05; ** <0.005; *** <0.001; **** <0.0001, one-way ANOVA test for all panels.

STAR+METHODS

KEY RESOURCES TABLE

REAGENT or RESOURCE	SOURCE	IDENTIFIER
Antibodies		
Mouse anti-Flag M2	Sigma-Aldrich	Cat# F1804 RRID:AB_262044
Goat anti-GST	GE Healthcare	Cat# 27457701 RRID:AB_771432
Mouse anti-SKIP	Santa Cruz	Cat# sc-393856 RRID: N/A
Mouse anti-beta-actin 1	Santa Cruz	Cat# sc-47778 RRID:AB_2714189
Rabbit anti-CDC40/PRP17	Abcam	Cat# ab175924 RRID:N/A
Rabbit anti-PPIL1	Proteintec	Cat# 15144-1-AP RRID:AB_2169603
Rabbit anti-CUX1	Santa Cruz	Cat# sc-13024 RRID:AB_2261231
Rat anti-CTIP2	Abcam	Cat# ab18465 RRID:AB_10015215
Rabbit anti–cleaved caspase3	Cell Signaling	Cat# 9661 RRID:AB_2341188
Rabbit anti-HA	Cell Signaling	Cat# 3724 RRID:AB_1549585
Rabbit anti-p53	Leica	Cat# P53-CM5P RRID:AB_2744683
Rabbit anti-PAX6	Biolegend	Cat# 901301 RRID:AB_2565003
Rabbit anti-TBR2	Abcam	Cat# ab183991 RRID:AB_2721040

Rabbit anti-γ-H2AX	Cell Signaling	Cat# 9718 RRID:AB_2118009
Mouse anti-SATB2	Abcam	Cat# ab51502 RRID:AB_882455
Rat anti-PH3	Abcam	Cat# ab10534 RRID:AB_2295065
Mouse anti-GAD65	Abcam	Cat# ab26113 RRID:AB_448989
Mouse anti-GAD67	Millipore	Cat# MAB5406 RRID:AB_2278725
Bacterial and Virus Strains		
BL21(DE3) *E. coli* cells	ThermoFisher	#C600003
Rosetta™(DE3) Competent *E. coli* Cells	Millipore	#ab70945
Biological Samples		
Skin punch biopsy	This paper	N/A
Chemicals, Peptides, and Recombinant Proteins		
Cyclosporin A	Cell Signaling	#9973
Bio-FAPEFGPENPFRT-NH2	Peptide Synthetics	This study
N-succinyl-Ala-Ala-Pro-Phe-p-nitroanilide	Sigma	#S7388
SUMO protease	MC-LAB	SP-100
Critical Commercial Assays		
Click-iT™ EdU Alexa Fluor™ 488 Flow Cytometry Assay Kit	ThermoFisher	#C10420
HPLC column	WATERS	C18
Mini-PROTEAN Tris-Tricine Gel	BIO-RAD	
cDNA Synthesis Kit	ThermoFisher	#1671
RNeasy Plus Mini Kit	QIAGEN	
RNAscope Multiplex Fluorescent Assays V2 kit	Advanced Cell Diagnostics	# 323100
Deposited Data		
Raw and analyzed data	This paper	
Experimental Models: Cell Lines		
HEK293T cells	ATCC	N/A
Control HAP1 cell	Horizon	C631
PPIL1 knockout HAP1 cell	Horizon	HZGHC005943c001
WT and *PPIL1*$^{A99T/A99T}$ MEF cells	This paper	N/A

Patient-derived skin fibroblast cells	This paper	N/A
Experimental Models: Organisms/Strains		
Mouse, C57BL/6J, *Ppil1* frameshift (1bp del)	This paper	N/A
Mouse, C57BL/6J, *Ppil1*^{A99T} knockin	This paper	N/A
Mouse, C57BL/6J, *Ppil1* HA-tag knockin	This paper	N/A
Mouse, C57BL/6J, *Ppil1*^{R55A} knockin	This paper	N/A
Mouse, C57BL/6J, Prp17^{P95A} knockin	This paper	N/A
Mouse, C57BL/6J, Prp17 frameshift knockin	This paper	N/A
Oligonucleotides		
Ppil1 knock-out mice, gRNA: GTCTGGTCCTGCGTTGGCCA	This paper	N/A
For the generation of patient mutation p.A99T knockin mice in *Ppil1*, gRNA: GTCTGGTCCTGCGTTGGCCA; single-strand repair DNA oligo: TGCCCTTCATGCTCTTCTCTCTCCTTAT GTCCCCAGGGGCTGGGATTC TCACGATGGCCAACGCAGGACCAGACA CCAATGGCAGCCAGTTCTTTGTGACC.	This paper	N/A
To generate *Ppil1* N-terminal HA epitope knockin mice, gRNA: GATACCTTCGCTCAGCATGG; single-strand repair DNA: CCGGGTTAACTCCGCCGGAAGTAGTGA TTGCTAGCGGGGGGGATACCTTCGCTC AGCATGTACCCATACGATGTTCCAGATT ACGCGTCTCTGGCGGCGATTCCCCCAG ACACCTGGCAGCCGCCCAACGTCTACC TGGAGACTAGGTGAG.	This paper	N/A
For the generation of patient mutation p.R131Q knockin mice in *Ppil1*, gRNA: TCCCTATACCCTGGCACACT; single-strand repair DNA oligo: GGTCCTGGGAGTTTGTTTCCACCATGC CCACTCGATTCACCATCCCTATACCCTG GCACACTTGTCCAAAAATAGTATGCTTG CCGTCCAGCCATTGCGTGGGGGCCAG GGTCACAAAGAAC.	This paper	N/A

To produce PRP17-p.P95A knockin and knockout mice, gRNA: TTCCTTATATCGTTGCAGTT; Single-strand repair DNA: GGATTAGAGTTGAAAATACATTGTAATT TCAGGATCCTTCTTTTCCTTCCTTATATC GTTGCAGTTTGGAGCAGAAAATCCCTTT CGAACACAGCAAATGGCTGCCCCTAGA AATATGCTTTCTGGGTATGCAGAGCCAG C.	This paper	N/A
To generate of *Ppil1*^{R55A} knockin mice, gRNA: TGAAGTCCTTGATGATCCTG; single-strand repair DNA oligo: GTCATTGTCCTGGAGCTATACTGGAAG CATGCGCCCAAGACCTGCAAGAACTTC GCGGAGCTGGCTCGGCGGGGCTACTA CAATGGCACCAAGTTTCACGCGATCATC AAGGACTTCATGATCCAAGGCGGCGAC CCGACAGGCACAGGTACACTTAAGCCA CCATTGGGGAGGAACTGGGTGGTAAGG CAGCCACAGCT.	This paper	N/A
CRISPRi scramble gRNA: GCACTACCAgaGCTAACTCA	This paper	N/A
CRISPRi *PRP17* gRNA 01: CTCACTGTCCGAGTCCGATT	This paper	N/A
CRISPRi *PRP17* gRNA 02: GGACCCTGAACCCGAACCAT	This paper	N/A
CRISPRi *PRP17* gRNA 03: GCGATTTAGTCAAGTGCATG	This paper	N/A
CRISPRi *PRP17* gRNA 04: GGCAGTGGACTCGGCTCCGG	This paper	N/A
Recombinant DNA		
pET22b-PPIL1	This paper	N/A
pET28b-His-SUMO-PRP17(18aa)	This paper	N/A
pGEX-6P1-GST-SKIP(aa59-129)	This paper	N/A
PX330-U6-2XBsmBI-gRNA-CBh-dCas9-KRAB-T2a-Puro	This paper	N/A
pLV-hU6-sgRNA hUbC-dCas9-KRAB-T2a-Puro	Addgene	#71236
pMD2.G envelope plasmid	Addgene	#12259
psPAX2 packaging plasmid	Addgene	#12260
pSPLICEEXPRESS-*Atg4d*	This paper	N/A
pSPLICEEXPRESS-*Evi5l*	This paper	N/A
Software and Algorithms		

Dynamic NMR (DNMR) module of the TopSpin 3.2 acquisition and processing software	Bruker	N/A
Origin 7	OriginLab Inc.	http://originlab.com
Graphpad Prism 7	Graphpad	https://www.graphpad.com/scientific-software/prism/
Adobe Illustrator	Adobe	N/A
Adobe Photoshop	Adobe	N/A
Inkscape	N/A	https://inkscape.org/
Image Lab	Bio-rad	http://www.bio-rad.com/en-us/product/image-lab-software?ID=KRE6P5E8Z
STAR	Dobin et al., 2013	https://github.com/alexdobin/STAR
DESeq2	Love et al., 2014	http://bioconductor.org/packages/release/bioc/html/DESeq2.html
rMATS 3.2.5	Shen et al., 2014	http://rnaseq-mats.sourceforge.net/rmats3.2.5/
Leafcutter	Li et al., 2018	https://davidaknowles.github.io/leafcutter/
WebLogo	Crooks et al., 2004	https://weblogo.berkeley.edu/logo.cgi
MaxEntScan	Yeo and Burge, 2004	http://hollywood.mit.edu/burgelab/maxent/Xmaxentscan_scoreseq_acc.html
Pymol	N/A	N/A
Other		

CONTACT FOR REAGENT AND RESOURCE SHARING

Further information and requests for resources and reagents should be addressed to and will be fulfilled by the Lead Contacts, Joseph Gleeson (jogleeson@ucsd.edu) or Eamonn Sheridan (e.sheridan@leeds.ac.uk).

EXPERIMENTAL MODEL AND SUBJECT DETAILS

Human subjects

All work with patients was approved by the UCSD IRB protocol 140028 or local protocols, and performed according to accepted guidelines. All patients and/or parents/guardians signed a consent form for participation. All mutations were confirmed with Sanger sequencing according to the base change and inheritance within the family.

Animals

All work with mice was performed in accordance with UCSD IACUC protocols. The mixture of gRNA (0.6 μM), Cas9 protein (0.6 μM, NEB, #M0646T), and single-strand DNA oligo (10 ng/μl, only for knockin) was injected to mouse zygotes at UCSD Transgenic Mouse Core, offspring genotyped by PCR Sanger sequencing. Mice with correct genotypes were backcrossed with C57BL/6J WT mice for at least two generations before breeding to generate homozygous mice for analyzing phenotypes.

To produce *Ppil1* knock-out mice (1 bp deletion, c.302delC; NM_026845.4), gRNA targeting GTCTGGTCCTGCGTTGGCCA was transcribed and purified as described previously (Ran et al., 2013). For the generation of patient mutation knockin mice in *Ppil1*$^{p.A99T}$, single-strand DNA oligo (TGCCCTTCATGCTCTTCTCTCTC CTTATGTCCC CAGGGGCTGGGATTCTCACGATGGCCAACGCAGGACCAGACACCAATGGCAGCC AGTTCTTTGTGACC) was co-injected with gRNA and Cas9 protein.

To generate *Ppil1* N-terminal HA epitope knockin mice, synthesized crRNA (0.6 μM) targeting GATACCTTCGCTCAGCATGG was co-injected with tracrRNA (0.6 uM, IDT DNA), Cas9 protein, and single-strand repair DNA (CCGGGTTAACTCCGCCGGAAGT AGTGATTGCTAGCGGGGGGGATACCTTCGCTCAGCATGTACCCATACGATGTTCC AGATTACGCTCTCTGGCGGCGATTCCCCCAGACACCTGGCAGCCGCCCAACGTCT ACCTGGAGACTAGGTGAG).

To generate patient mutation *Ppil1*$^{p.R131Q}$ knockin mice, synthesized crRNA targeting TCCCTATACCCTGGCACACT was co-injected with tracrRNA, Cas9 protein, and single-strand repair DNA (GGTCCTGGGAGTTTGTTTCCACCATGCCCACTCGATT CACCATCCCTATACCCTGGCACACTTGTCCAAAAATAGTATGCTTGCCGTCCAGCC ATTGCGTGGGGGCCAGGGTCACAAAGAAC).

To produce *Prp17*$^{p.P95A}$ knockin mice, synthesized crRNA targeting TTCCTTATAT CGTTGCAGTT was co-injected with tracrRNA, Cas9 protein, and single-strand repair DNA (GGATTAGAGTTGAAAATACATTGTAATTTCAGGATCCTTCTTTTCCTTCCTTAT ATCGTTGCAGTTTGGAGCAGAAAATCCCTTTCGAACACAGCAAATGGCTGCCCCTA GAAATATGCTTTCTGGGTATGCAGAGCCAGC). Besides *Prp17*$^{p.P95A}$ knockin mice, we also got a *Prp17* frameshift mouse (11 bp deletion, c.277_287delTTTGGACCAGA; NM_027879.2) and was bred to homozygosity after back-crossing with WT mice.

To generate *Ppil1*$^{p.R55A}$ knockin mice, synthesized crRNA (0.6 μM) targeting TGAAGTCCTTGATGATCCTG was co-injected with tracrRNA (0.6 μM, IDTDNA), Cas9 protein, and single strand repair DNA (GTCATTGTCCTGGAGCTATACTGGAAGCATGC

GCCCAAGACCTGCAAGAACTTCGCGGAGCTGGCTCGGCGGGGCTACTACAATGG
CACCAAGTTTCACGCGATCATCAAGGACTTCATGATCCAAGGCGGCGACCCGACA
GGCACAGGTACACTTAAGCCACCATTGGGGAGGAACTGGGTGGTAAGGCAGCCA
CAGCT).

Mammalian Cells

Dermal punch biopsy was obtained under UCSD IRB protocol 171094, patients underwent sterile 0.5cm biopsy, which was mechanically dissociated and then cultured in 20% FBS in DMEM and 100U/ml penicillin-streptomycin until confluent as described (Vangipuram et al., 2013). Cells at low passage were used for protein expression analysis. HEK293T were cultured in DMEM supplemented with 10% FBS, 2mM L-glutamine and 100U/ml penicillin-streptomycin. Mouse embryonic fibroblast (MEF) cells were isolated from E13.5 embryos using mouse embryonic fibroblast isolation kit (ThermoFisher, #88279) and cultured in DMEM supplemented with 10% FBS, 2mM L-glutamine and 100 units/ml penicillin-streptomycin on gelatin-coated dishes. PPIL1 knockout HAP1 cells was generated in Horizon using the CRISPR/Cas9 system, and carries a 22 bp deletion in the first exon (22 bp deletion, c.28_49del, NM_016059). HAP1 cells were grown in Iscove's Modified Dulbecco's Medium (IMDM) with 10% FBS and 100 units/ml Pen/Strep.

METHOD DETAILS

Analysis of patient phenotype

Patients were recruited as part of a multiyear effort to identify pedigrees showing multiple affected children with neurodegenerative or neurodevelopmental phenotypes, in the presence of parental consanguinity, in order to identify causes of recessive pediatric brain disease. Families were recruited at several locations around the world including the US, UK, Egypt, Pakistan, and Turkey. Subjects underwent detailed phenotyping analysis including standard medical, genetic, and neurological evaluations, serial evaluations over the course of months to year to characterize the natural history of disease progression, pedigree analysis, exclusion of previously identified genetic syndromes through the use of the London Dysmorphology Database and OMIM, followed by brain MRI or CT scan to evaluate for structural defects, and candidate gene sequencing where appropriate to exclude previously reported syndromes. Phlebotomy was performed on the entire family including all genetically informative members, for segregation analysis and linkage.

Human Brain MRI

Imaging was performed on standard clinical radiology equipment (0.5-1.5T) GE instruments, using standard T1, T2, and FLAIR settings. Hard copies of brain images were available in all cases, whereas digital files were available on a minority. This precluded quantitative analysis of brain morphology but allowed for comparison of images in the sagittal, axial and coronal orientations.

DNA extraction, whole-exome, and whole-genome sequencing

Patient DNA extraction and whole-exome sequencing libraries were performed using the Agilent SureSelect Human All Exon v2.0 (44Mb baited target) and sequenced on an Illumina HiSeq 2500 with v2 chemistry (Read Length: 151). Variant calling and filtering were performed using in-house software with Annovar, Variant Effect Prediction software

to define population-specific allele frequencies from 1000 Genomes, the Greater Middle East Variome, dbSNP, and gnomAD. Variants were prioritized according to allele frequency, conservation, and predicted effects on protein function.

Variant prioritization

Variant calling and filtering were performed following an established exome sequencing pipeline (Lee et al., 2019). Identified variants were filtered out if not consistent with recessive monogenic inheritance, if the minor allele frequency (MAF) of gnomAD was >1:10,000, if MAF of local cohort was > 1:1,000, if not moderate or high impact, if CADD PHRED score ≤20, or if not predicted as damaging by either SIFT, PolyPhen, or MutationTaster.

Sanger sequencing

Primers for Sanger sequencing were designed using the Primer3 program (U. Massachusetts) and tested for specificity using the Alamut Visual 2.7.1 software. PCR products were treated with Exonuclease I (Fermentas) and Shrimp Alkaline Phosphatase (USB Corp) and sequenced using the Big Dye terminator cycle sequencing kit v.3.1 (Applied Biosystems) on an ABI DNA analyzer (Applied Biosystems). Sequence data were analyzed using Snapgene software.

PPIL1 protein expression and purification

Full-length PPIL1 (GenBank NM_016059.4) open reading frame was cloned into NdeI/ XhoI sites in pET22b expression vector. Plasmids were transformed into BL21(DE3) *E. coli* cells, grown at 37 ˚C in 2YT media (5 g/l NaCl, 10 g/l yeast extract, 16 g/l tryptone), or M9 minimal media supplemented with 0.05% w/v ^{15}N NH_4Cl (for ^{15}N labelled protein), with 100 µg/ml ampicillin. Protein expression was induced using 1 mM isopropyl β-D-1-thiogalactopyranoside (IPTG) at OD_{600} 0.5-0.8 and subsequently incubated at 18 ˚C overnight. PPIL1 protein was purified from cell lysate using a 1 ml Ni-NTA column (GE Healthcare) and eluted using an imidazole gradient (10 mM to 500 mM imidazole, 0.5 M NaCl, 20 mM sodium phosphate). Purity and identity of purified proteins were confirmed using SDS-PAGE Western analysis with an anti-PPIL1 antibody, and mass spectrometry.

Protein aggregation assay

Protein unfolding and aggregation were measured over a temperature gradient using an Optim machine (Unchained Labs). Protein unfolding was assessed using the barycentric mean wavelength of intrinsic protein fluorescence. Fluorescence was excited using a laser at 266 nm and emission monitored from 280 nm to 450 nm. Protein aggregation was detected by measuring static light scattering at 266 nm. Assays were carried out in PBS buffer (pH 7.4).

Immunoprecipitation assay and western blotting

HEK293T cells were seeded into 6-well plates and transfected with indicated plasmids using Lipofectamine 2000. 36 h after transfection, cells were lysed in RIPA buffer with protease inhibitor cocktail (Roche Applied Science, 11836170001). Cell lysates were centrifuged at 14,000g for 15 min at 4 °C. 45 µl supernatant was mixed with 15 µl 4× SDS-loading buffer and further heated at 95 °C for 2 min as total lysates. The remaining

supernatant was incubated with 10 µl prewashed anti-FLAG M2 magnetic beads (Sigma-Aldrich, M8823) for 3 hours at 4 °C. The beads were washed four times with lysis buffer and eluted in 40 µl 2× SDS-loading buffer. Total lysates and immunoprecipitates were further separated by SDS-PAGE and analyzed by immunoblotting. Primary antibodies used include mouse anti-Flag M2 (1:10,000, Sigma-Aldrich, F1804), mouse anti-SKIP (1:1,000, Santa Cruz, sc-393856), mouse anti-beta-actin (1:1,000, Santa Cruz, sc-47778), rabbit anti-CDC40/PRP17 (1:2,000, Abcam, ab175924) and rabbit anti-PPIL1 (1:2,000, Proteintech, 15144-1-AP).

SKIP protein expression and purification

SKIP 59-129 was cloned into pGEX-6P1 expression vector (linearised using SalI and NotI restriction enzymes) using In-Fusion HD cloning kit (Clontech). The vector was transformed into BL21(DE3) Escherichia coli cells and grown at 37 ˚C in 2YT media (100 µg/ml ampicillin). SKIP 59-129 expression was induced with 1 mM isopropyl β-D-1-thiogalactopyranoside (at OD_{600} 0.5-0.8) for three hours at 37 ˚C. 1 ml glutathione sepharose columns (GE Healthcare) were used to purify GST-SKIP 59-129 from cell lysates and protein was eluted with a 10 ml glutathione injection (10 mM glutathione, 50 mM Tris-HCl pH 7.4).

Surface plasmon resonance (SPR) assay

Anti-GST antibodies were immobilized on a CM5 chip (GE Healthcare) using an amine coupling reaction, in 100 mM sodium acetate buffer (pH 5.6). The chip surface was activated using 35 µl, 0.05 M N-hydroxysuccinimide/ 0.2 M N-ethyl-N'-(dimethylaminopropyl) carbodiimide injections (GE Healthcare amine coupling kit). 20 µl anti-GST antibody (GE healthcare, 27457701) was injected at 30 µg/ml and unreacted material was subsequently eluted with 40 µl 1 M NaCl. Unreacted sites were capped using 35 µl 1 M ethanolamine·HCl pH 8.5. Amine coupling was performed in 100 mM sodium acetate running buffer (pH 5.6). N-terminal GST tagged SKIP 59-129 protein was injected across the chip surface to allow immobilization on anti-GST antibodies. In order to measure binding, PPIL1 proteins were injected across the chip surface (50 µl/min, 2.5 minutes) in PBS, 0.05 % v/v IGEPAL running buffer. Experiments were carried out using Biacore 3000 system at 25°C and the data were analyzed using Biacore BiaEvaluation software.

Nissl staining

Dissected mouse brains were fixed overnight in Bouin's solution and embedded in paraffin. Sagittal sections were collected at a thickness of 5 µm and stained with Cresyl violet after deparaffinization and rehydration. Images were taken using a Leica Aperio AT2 scanner and a Keyence BZX-700 microscope.

Immunofluorescent staining and Fluorescence *in situ* Hybridization

Embryos were fixed in 4% paraformaldehyde (PFA), cryoprotected in 30% sucrose and then cryosectioned for immunostaining. Primary antibodies and reagents used include: rabbit anti-CUX1 (1:100, Santa Cruz, sc-13024), rat anti-CTIP2 (1:300, Abcam, ab18465), rabbit anti–cleaved caspase3 (1:400, Cell Signaling, 9661), rabbit anti-HA (1:300, Cell Signaling, 3724), rabbit anti-P53 (1:500, Leica, P53-CM5P), rabbit anti-PAX6 (1:300,

Biolegend, 901301), rabbit anti-TBR2 (1:1,000, Abcam, ab183991), Rabbit anti-γ-H2AX (1:400, Cell Signaling, 9718), Mouse anti-SATB2 (1:400, Abcam, ab51502), and Goat anti-SOX2 (1:400, R&D systems, AF2018).

Fluorescence *in situ* Hybridization (FISH) was performed following the manufacturer's instructions (Advanced Cell Diagnostics) of RNAscope Multiplex Fluorescent Assays V2 kit. TUNEL staining was performed with Apoptag Fluorescein *in situ* apoptosis kit (Millipore, S7110) following the provided manual. EdU fluorescence staining was performed with Click-iT™ EdU Alexa Fluor™ 488 Flow Cytometry Assay Kit (ThermoFisher, C10420). Images were taken using a Zeiss LSM 880 confocal microscope and Keyence BZX-700 fluorescent microscope and analyzed with Adobe Photoshop and Illustrator.

RNA-sequencing and data analysis

Total RNA was extracted from cultured cells or dissected mouse tissues following the manual of RNeasy Plus Mini Kit (Qiagen), yield and quality of RNA assessed by NanoDrop (Thermo Fisher Scientific) and Agilent Bioanalyzer (Agilent Technologies), respectively, enriched by poly-A capture. Paired-end libraries were prepared according to the manufacturer's protocols (TruSeq Stranded mRNA, Illumina) and sequenced using Illumina HiSeq2500 or 4000 system (paired-end 100, Illumina). 80-100 million reads were collected for each sample.

rMATS computational analysis

FASTQ files containing RNA-seq data from WT and mutant samples were trimmed with Cutadapt(Martin, 2011), aligned to reference human hg19 or mouse (GRCm38) with GTF release M16 using STAR aligner(Dobin et al., 2013) with ENCODE standard options, and with 'end-to-end alignment type' checked as required by rMATS (Shen et al., 2014). Alternative splicing events were summarized by rMATS 3.2.5, with 'novel splice site detection' turned on. Heatmap representation of inclusion levels for each sample was plotted using R package pheatmap(Kolde and Kolde, 2015). All intron positions for mouse were downloaded as one BED file from UCSC browser. Sequences from the mouse genome file were extracted using known start and end positions with bedtools getfasta function(Quinlan and Hall, 2010). Then the length and GC-content distributions of all introns, as well as introns residing in alternative splicing events, were calculated in R ggplot2(Wickham, 2016), with significance determined by FDR <0.05 and the absolute value of inclusion level difference > 0.05. A one-sided Mann-Whitney test was performed to obtain *p*-value between each group. Sequences of 40bp in length (19bp extension towards each direction) around 5' and 3' consensus splice sites of all mouse introns as well as our splicing event introns were extracted and stacked as sequence logo plots using WebLogo(Crooks et al., 2004). Splice sites strength was calculated using maxentpy python wrapper for MaxEntScan(Yeo and Burge, 2004) for both 5' and 3' sites, and scores plotted in R.

Leafcutter computational analysis

LeafCutter release 0.2.8 with STAR aligned bam files were performed according to published methods (Li et al., 2018). Intron clustering was performed by leafcutter_cluster.py with default options (maximum intron length as 100,000 bp,

minimum reads in a cluster as 10, and the minimum fraction of reads in a cluster that support a junction as 0.001, respectively). Differential intron excision analysis was performed by leafcutter_ds.R with default options but --min_coverage=30 to increase specificity and --min_samples_per_intron=3 as recommended. Significance was determined by adjusted *p*-value (FDR) < 0.05 from the final output.

Sashimi plot

Sashimi plots were generated with python script rmats2sashimiplotm, with sorted BAM files from STAR used as inputs. Event files contain selected events extracted from rMATS outputs. Plots for different splicing types were specified by -t argument.

Enrichment analysis for misspliced genes in diseases

rMATS output produced lists containing the genes of significant events (misspliced genes) and genes in non-significant events (un-misspliced genes). Brain AS genes (n=16052) derived from (Yan et al., 2015b), OMIM genes associated with neurodevelopmental disorders (n=2755), cancer (n=589), cardiac/heart disease (n=446), and immune disorders (n=386) derived were requested from NCBI.

A 2x2 contingency table was generated for each disease gene list and the number of genes was calculated for inclusion or exclusion in the misspliced and un-misspliced genes, respectively, or calculated with 95% confidence interval. *p*-values were generated using Fischer's Exact test and corrected for multiple tests with the Bonferroni method.

Pathway and Process Enrichment Analysis

Enrichment of Gene Ontology (GO) Biological Processes and KEGG pathways was carried out with KOBAS 2.0 as previous described(Xie et al., 2011). The list of genes (n = 2134) with altered AS in the mutant mouse brains were created from all the significant AS events in rMATS analysis. All expressed genes (n = 15169) in E14.5 mouse brain hemisphere were obtained from RNA-seq data with RPKM>1.0 and used as a background list. Networks of enriched pathways were generated by Metascape(Zhou et al., 2019), with ontology sources: GO Biological Processes, KEGG Pathway, Reactome Gene Sets, and CORUM. Terms with a $p < 0.01$, a minimum count of 3, and an enrichment factor > 1.5, grouped into clusters based on membership similarities.

Semi-quantitative RT-PCR

Total RNA was extracted from cultured cells or tissue with RNeasy Plus Mini Kit (Qiagen), according to the manufacturer's instructions. 1 μg RNA was reverse transcribed with cDNA Synthesis Kit (Maxima First Strand cDNA Synthesis Kit for RT-qPCR, with dsDNase, ThermoFisher) following the provided manual. Minus reverse transcription (RT) negative control was added for each sample to check for DNA contamination. Negative control for PCR was included for each experiment. Primers sequences used were listed in Table S5.

Splicing reporter assay

Splicing minigene constructs were generated as previously reported (Kishore et al., 2008). Briefly, DNA fragment containing 3' intron-exon-intron-exon-5' intron was amplified by PCR using mouse genomic DNA as a template, which was further cloned into

pSpliceExpress reporter vector using gateway recombination cloning technique. For splicing analysis, cells were transfected with pSpliceExpress plasmids and cultured for additional 36-48 hours before the extraction of total RNA. RNA was then reversed transcribed and semi-quantitative RT-PCR was performed to check the splicing of the introns. Primer sequences were: CTCTCTACCTGGTGTGTGGG (forward), and AGTGCCAAGGTCTGAAGGTC (reverse). *GADPH* was amplified as control for each experiment.

Purification of uniformly ^{15}N labeled PRP17 peptide

His-SUMO-PRP17 (18 mer: T84-T101, TYETMFAPEFGPENPFRT) was cloned into NcoI/XhoI sites in pET-28b expression vector, transformed into BL21(DE3) *E. coli* cells, grown in 5 ml LB medium at 37˚C for 6 hours and 500 µl cultured LB medium was then added to 100 ml M9 minimal media supplemented with 0.05% w/v ^{15}N NH_4Cl for overnight culture at 37 ˚C. Cells were further transferred to 4 L ^{15}N minimal medium. Protein expression was induced using 1 mM IPTG at OD_{600} 0.7-0.8 and cells were subsequently incubated at 37 ˚C for 8 hours. The His-tagged recombinant protein was purified from cell lysates using Ni-NTA agarose (GE healthcare) and eluted protein was further dialyzed into SUMO cleavage buffer (25mM Tris-HCl, 100 mM NaCl, PH=8.0). Purified protein was cleaved by SUMO protease (MC-LAB, SP-100) at 30 ˚C for 6 hours. After cleavage, His-SUMO and SUMO proteases were absorbed by Ni-NTA agarose and the collected flow-through containing PRP17 peptide was loaded to reverse-phase HPLC column (WATERS, C18) with 0.1% TFA (Trifluoroacetic acid). The peptide was eluted using an increased gradient of elution buffer (90% Acetonitrile, 0.1% TFA, and 10% H_2O). Purified ^{15}N labeled PRP17 peptide was collected and further lyophilized. Purity and identity of purified peptide were confirmed using peptide SDS-PAGE with 16.5% Mini-PROTEAN Tris-Tricine Gel (BioRad, Inc), MALDI-TOFMS analysis for molecular weight, and mass spectrometry.

^{1}H ^{15}N HSQC of PPIL1

^{1}H ^{15}N heteronuclear single quantum coherence (HSQC) spectra of ^{15}N labeled PPIL1 were recorded in the presence and absence of PRP17 peptide (Bio-FAPEFGPENPFRT-NH_2; purchased from Peptide Synthetics, Inc). PPIL1 concentration was 80 µM and PRP17 peptide was titrated in at 0-5 molar equivalents in 10 mM sodium phosphate, 100 mM NaCl, 5% D_2O at pH 6.5. Spectra were collected on a Bruker 600 MHz NMR spectrometer equipped with a quadruple-resonance QCI-P cryo-probe (QCI-P CP). Resonances were identified using the published assignment of PPIL1 (Stegmann et al., 2010; Xu et al., 2005). Average chemical shift perturbations were calculated as described elsewhere (Hewitt et al., 2017).

^{1}H ^{15}N H(Cα)N ZZ exchange spectra of PRP17 peptide

^{1}H ^{15}N-H(Cα)N ZZ exchange spectra (based on spectra used by previous study (Dujardin et al., 2015)) were acquired of 500 µM PRP17 (residues 89-101 PRP17, Ac-FAPEFG**P**ENPFRT-NH_2, ^{15}N, and ^{13}C labeled Pro95) in the presence and absence of catalytic concentrations of PPIL1 (5 µM). The sample buffer used was PBS buffer (pH 7.4), 5% D_2O and spectra were acquired using a 950 MHz triple resonance spectrometer equipped with a TXO triple resonance cryo-probe (TXO-CP).

^{1}H ^{15}N ZZ exchange spectra of uniformly ^{15}N labeled PRP17 peptide

^{1}H ^{15}N ZZ exchange spectra were acquired of uniformly ^{15}N labeled PRP17 peptide (residues 84-101 PRP17; 400 µM) in the presence and absence of catalytic concentrations of PPIL1 (4 µM). Mixing times used were 10, 20, 40, 60, 80, 100, 120(x2_, 150, 200, 250(x2), 350, 450, 600 and 750 ms. The sample buffer used was: 25 mM sodium phosphate buffer, 100 mM NaCl, 1 mM dithiothreitol, 5% D_2O at pH 7.0. Spectra were acquired on a Bruker 950 MHz NMR spectrometer with a TXO triple resonance cryo-probe (TXO-CP).

Isothermal Titration Calorimetry (ITC) assay

PRP17 peptide (2 mM) was titrated into PPIL1 WT protein (40 µM), in PBS buffer (pH 7.4). Experiments were carried out using Microcal ITC 200 calorimeter at 25 ˚C. PRP17 titrations were carried out using 2 µl, 4-second injections spaced 2 minutes apart. Results were analyzed using Microcal Origin 7 software. Binding curves were fit to a one-site interaction model using a fixed stoichiometry (n = 1), which is recommended for low-affinity interactions(Turnbull and Daranas, 2003).

Assignment of cis and trans resonances, PRP17 peptide

A ^{1}H-^{13}C heteronuclear single quantum coherence (HSQC) spectrum of PRP17 peptide (PRP17 89-101; ^{13}C and ^{15}N labeled pro95) were recorded with 500 µM peptide in PBS (pH 7.4), 5 % v/v D_2O using a Bruker 750 MHz NMR spectrometer equipped with a triple-resonance TCI triple resonance cryoprobe (TCI-CP). *Cis* and *trans* PRP17 Gly94-Pro95 peptide bond assignment was based on the ^{13}C chemical shift for C_γ and C_β resonances, as reported (Shen and Bax, 2010).

CRISPRi knockdown assay in HEK293T cells

Empty CRISPRi plasmid (PX330-U6-2XBsmBI-gRNA-CBh-dCas9-KRAB-T2a-Puro) was generated on the modified PX330 with 2x BsmBI gRNA cloning sites. dCas9-KRAB-T2a-Puro was amplified from vector pLV-hU6-sgRNA-hUbC-dCas9-KRAB-T2a-Puro (Addgene #71236) and cloned inside PX330 to replace original WT Cas9. gRNAs targeting PRP17 or scramble gRNA was further cloned between 2XBsmBI sites. CRISPRi plasmids containing *PRP17* or scramble gRNAs were co-transfected into HEK293T cells with either empty pcDNA3 or PRP17 cDNAs. 24 hours after transfection, cells were treated with 5 µg/ml puromycin for 36 hours to kill untransfected cells and then cultured in medium without puromycin for additional 24-36 hours before used for RNA extraction or Resazurin cell viability assay.

Resazurin (cell viability/proliferation) assay

Cultured cells were treated with 20% Resazurin (R&D, AR002) in the medium for 2 hours at 37 °C. 100 µl resazurin medium was further transferred to a well in 96-well plate. Fluorescence was read using Ex544nm/Em590 nm by Spectramax M5 microplate reader (Molecular Devices) and the final reading was subtracted from the background control (Resazurin in medium without cells).

Splicing rescue assay in HAP1 cells

WT and PPIase-inactive (p.R55A) *PPIL1* CDS with a stop-codon was cloned into Doxycycline (DOX)-inducible pINDUCER20 expression vector, using Gateway cloning system (ThermoFisher). Lentivirus was generated by co-transfecting pINDUCER20 (empty, WT *PPIL1*, and R55A *PPIL1*, respectively), pMD2.G envelope plasmid (Addgene 12259) and psPAX2 packaging plasmid (Addgene 12260) into HEK293T cells, using Lipofectamine 2000 (ThermoFisher Scientific). The viral supernatant medium was collected at 48 and 72 hours, respectively, and then pooled and concentrated 100x using Lenti-X Concentrator (Clontech, # 631232). WT and *PPIL1* knockout HAP1 cells were infected with concentrated lentivirus overnight in the presence of 5 μg/ml polybrene. 72 hours after infection, cells were selected with 1 mg/ml G418 for 2 weeks. Stable HAP1 cells were further treated with different concentrations of DOX (0, 0.1, and 0.5 μg/ml, respectively) for 72 hours and then lysed in RIPA buffer. Western blot was then applied to test the expression level of DOX-induced WT and R55A PPIL1. For splicing minigene assay, stable HAP1 cells were first cultured with 0.1 μg/ml DOX for 5 days and then transfected with the minigene splicing plasmid using lipofectamine 3000 (ThermoFisher Scientific) in the presence of DOX. Total RNA was extracted from transfected HAP1 cells 48 hours later and then reverse transcribed followed by semi-quantitative RT-PCR. For checking the splicing of endogenous genes, stable HAP1 cells were cultured in the presence of 0.1 μg/ml DOX for 7 days and then lysed for total RNA extraction, reverse transcription and semi-quantitative RT-PCR.

QUANTIFICATION AND STATISTICAL ANALYSIS

Unless specifically stated, each experiment was performed at least twice for each condition. Due to variabilities in the absolute values obtained in each experiment, for some assays, data from one experiment is presented and noted in the figure legend. For normally distributed data, unpaired t-tests were performed using Graphpad Prism 7 and *p* values were labeled in the figure panels with ns ($p > 0.05$), *($p < 0.05$), **($p < 0.01$), ***($p < 0.001$), and ****($p < 0.0001$), and the exact values were shown in either panels or figure legends. Other statistics used include one-way ANOVA test, non-parametric Mann-Whitney test, Wilcox test, and Fischer's Exact test, and were described in the figure legend and methods.

Supplemental Information

Mutations in spliceosomal genes *PPIL1* and *PRP17* cause neurodegenerative pontocerebellar hypoplasia with microcephaly

Guoliang Chai[1*], Alice Webb[2*], Chen Li[1], Danny Antaki[1], Sangmoon Lee[1], Martin W. Breuss[1], Nhi Lang[1], Valentina Stanley[1], Paula Anzenberg[1], Xiaoxu Yang[1], Patrick Gaffney[3], Klaas J. Wierenga[4], Brian Hon-Yin Chung[5], Mandy Ho-Yin Tsang[5], Lynn S. Pais[6], Alysia Kern Lovgren[6], Grace E. VanNoy[6], Heidi L. Rehm[6], Ghayda Mirzaa[7], Eyby Leon[8], Jullianne Diaz[8], Alexander Neumann[9], Lars Kuhn[10], Arnout Kalverda[10], Iain Manfield[10], David A Parry[2], Clare V Logan[2], Colin Johnson[2], David T Bonthron[2], Elizabeth MA Valleley[2], Patricia Jennings[11], Maha S. Zaki[12], Eamonn Sheridan[2], Joseph G. Gleeson[1]

Figure S1-S7

Table S1. Clinical information of all the affected individuals, related to Table 1

Table S2. Clinical variants table, related to Table 1

Table S3. Summary of altered RNA splicing events in *PPIL1* KO HAP1 cells using rMATS and Leafcutter, related to Figure 4

Table S4. Summary of the eight cyclophilin PPIases in the spliceosomal complexes, related to Figure 5

Table S5. Primer Sequences for RT-PCR, Related to Method Details

Movie S1. Visualization of PPIL1 and its interacting proteins in the cryo-EM structure of the spliceosome C* complex, related to Figure 5 and Figure 6

Cryo-EM structure of spliceosome C* complex (PDB: 5XJC), rotating around y- (first half) and x-axis (second half). The backside of PPIL1 (surface in teal) associates with the N-terminal of SKIP (surface in slate blue), and RBM22 (surface in orange), while its enzymatic side associates with the N-terminal of PRP17 (surface in purple). U5 snRNA (light blue) associates with the 5' exon junction, and U6 snRNA (green) forms a duplex with the 5' splice site (5'SS). RMB22 associates with the intron downstream 5'SS, which traverses a positively charged channel within the N-terminal domain of RBM22. U2 snRNA (light orange) forms a duplex with branching point site (BPS) region, which binds to the C-terminal WD40 domain of PRP17. PPIL1 is positioned to stabilize these associations within the spliceosome.

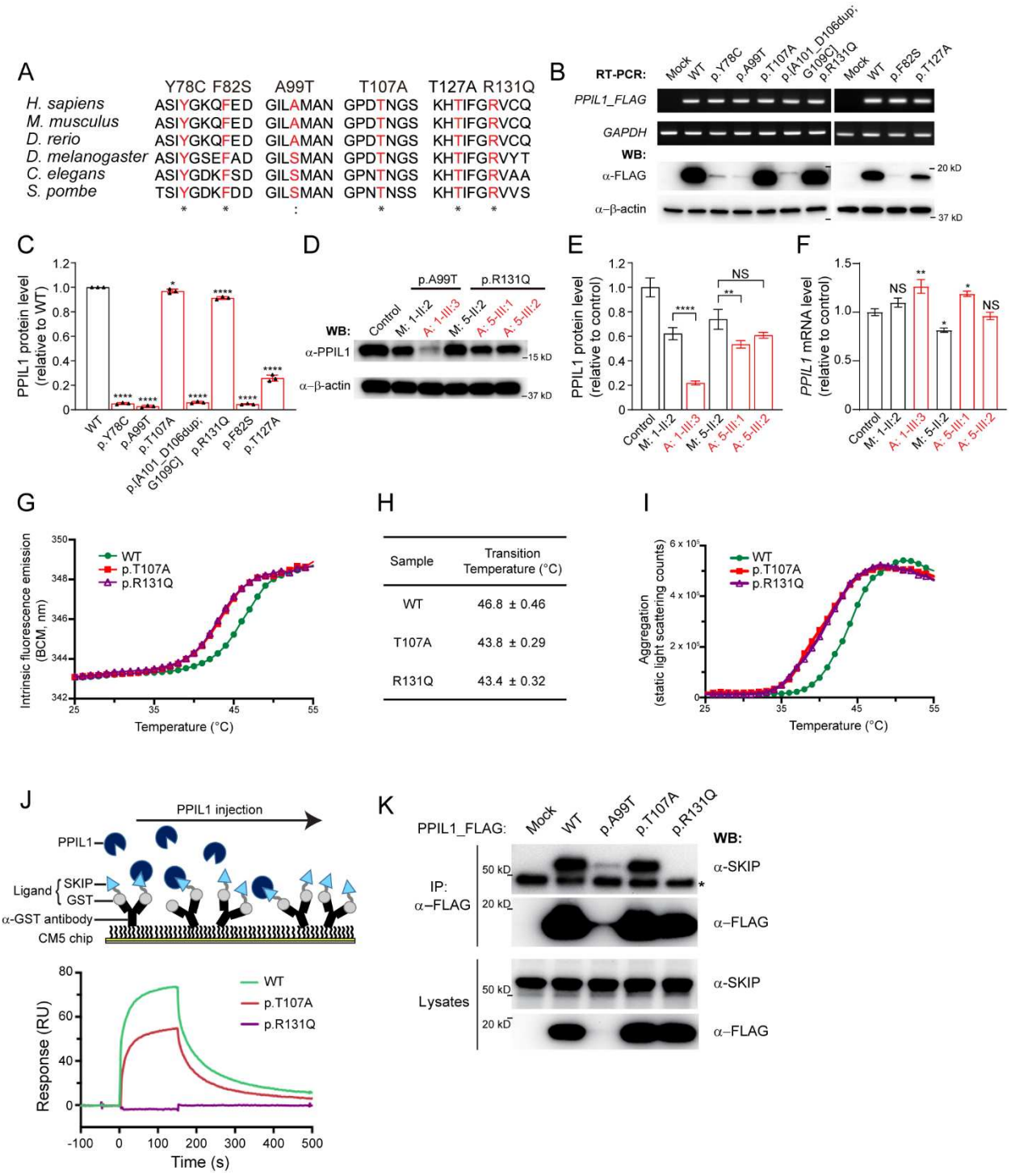

Figure S1. Patient mutations impair PPIL1 functions, related to Figure 1.

(A) Protein sequence alignment of PPIL1 shows mutated residues are highly conserved across eukaryotes. * stands for identical residues, : indicates similar residues.

(B) Overexpression of C-terminal FLAG-tagged WT and PPIL1 variants in HEK293T cells. Semi-quantitative RT-PCR: similar levels of RNA expression. Western blot: all patient mutations except p.T107A and p.R131Q show reduced PPIL1 protein level.
(C) Quantification of overexpressed Flag-tagged PPIL1 proteins. n = 3 for each condition.
(D and E) Western blot analysis (E) and quantification (F) of endogenous PPIL1 protein in dermal fibroblasts. n = 3 for each condition.
(F) RT-qPCR quantification of endogenous *PPIL1* mRNA expression in human dermal fibroblasts from control, mother (M), and affected (A, in red) from Family 1 and 5. n = 3.
(G-I) Protein unfolding and aggregation assay of WT and mutant PPIL1 proteins in PBS.
(G) The measurement of PPIL1 protein unfolding over a temperature gradient based on shifts in the barycentric mean wavelength of intrinsic protein fluorescence. (H) Mean transition temperatures of three experimental replicates, using different preparations of protein, are shown with standard deviation error. (I) The measurement of PPIL1 protein aggregation over a temperature gradient using static light scattering.
(J) Surface plasmon resonance (SPR) binding assay between PPIL1 and GST-SKIP fragment 59-129. Top: schematic of SPR assay. Bottom: Binding curves of WT (green), p.T107A (red), and p.R131Q (purple) PPIL1 proteins (1 μM) to SKIP 59-129. p.R131Q abolished and p.T107A reduced the interaction between PPIL1 and SKIP.
(K) Immunoprecipitation (IP) assay shows the interaction between PPIL1-Flag and endogenous SKIP in HEK293T cells. p.R131Q abolished the interaction between PPIL1 and SKIP. Asterisk: IgG heavy chain.
Mean ± s.d. *p*-value: NS > 0.05; * <0.05; ** <0.005; *** <0.001; **** <0.0001, one-way ANOVA test.

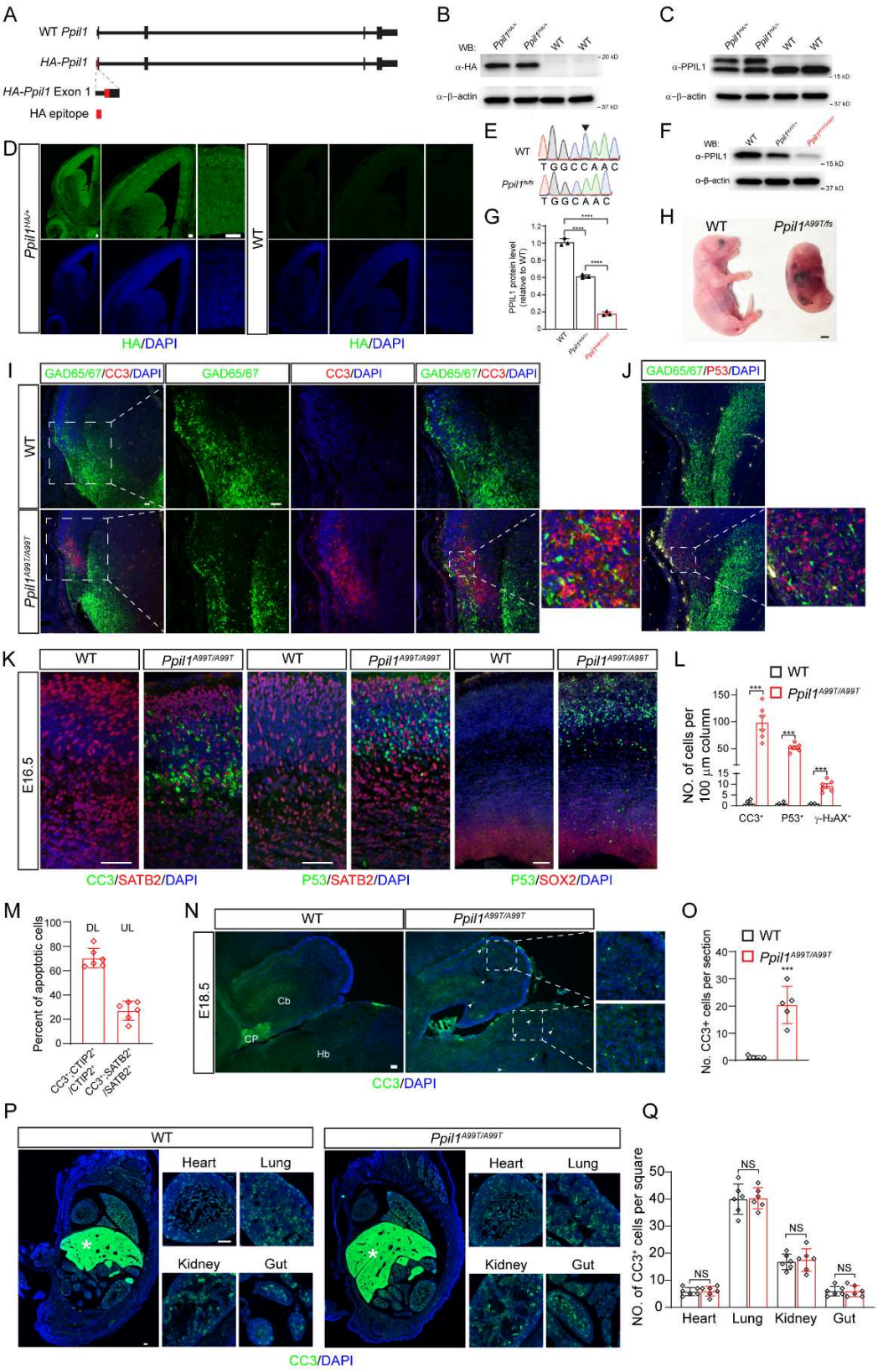

Figure S2. PPIL1 is required for brain development, related to Figures 2 and 3.

(A) Schematic view of the generation of N-terminal HA-tag knockin (KI) mice in *Ppil1* using CRISPR/Cas9 system.
(B and C) Western blot analysis of the expression of HA-tagged PPIL1 in E14.5 brains of $Ppil1^{HA/+}$ mice.
(D) Coronal sections of E14.5 embryos from $Ppil1^{HA/+}$ (top) and WT (bottom) embryos immunostained with an anti-HA antibody showing ubiquitous expression of PPIL1.
(E) Sanger sequencing traces showing homozygous 1 bp deletion (c.302delC; NM_026845.4) in $Ppil1^{fs/fs}$ embryo.
(F and G) Western blot analysis (F) and quantification (G) of endogenous PPIL1 protein in E14.5 WT, $Ppil1^{A99T/+}$, and $Ppil1^{A99T/A99T}$ embryos. n = 3 for each genotype. Mean ± s.d. **** p <0.0001, one-way ANOVA test.
(H) E18.5 compound heterozygous $Ppil1^{A99T/fs}$ embryos showing widespread phenotypes across the body.
(I and J) Coronal sections of E14.5 brain from WT and $Ppil1^{A99T/A99T}$ embryos stained for GAD65/67 (green) and CC3 (red in I) or P53 (red in J).
(K) Coronal sections of E16.5 cortex from WT and $Ppil1^{A99T/A99T}$ stained for DAPI (blue), CC3 (green, left), P53 (green, middle and right), SATB2 (upper layer neurons, red, left and middle), and SOX2 (neural stem cells, red, right).
(L) Quantification of $CC3^+$, $P53^+$, and γ-H_2AX^+ cells per 100 μm column in E16.5 WT and $Ppil1^{A99T/A99T}$ cortex. n = 3 embryos for each genotype. Mean ± s.d. *** p < 0.001, one-way ANOVA test.
(M) Quantification of percent of apoptotic upper ($P53^+$; $SATB2^+$) and deep ($P53^+$; $CTIP2^+$) layer neurons in E16.5 $Ppil1^{A99T/A99T}$ cortex.
(N) Sagittal sections of E18.5 brain from WT and $Ppil1^{A99T/A99T}$ stained for CC3 (green) and DAPI (blue). Arrows: apoptotic cells. Cb: cerebellum; Hb: hindbrain; CP: choroid plexus.
(O) Quantification of apoptotic cells per section of E18.5 WT and $Ppil1^{A99T/A99T}$ cerebellum. n = 3 embryos per genotypes. Mean ± s.d. *** p < 0.001, unpaired t-test.
(P) Sagittal sections of E16.5 WT and $Ppil1^{A99T/A99T}$ embryos stained for CC3 (green) and DAPI (blue). H, heart; L, lung; K, kidney; and G, gut. Asterisk: Autofluorescence in the liver.
(Q) Quantification of CC3+ cells per square (300 μm by 300 μm) in different organs from E16.5 WT and $Ppil1^{A99T/A99T}$ embryos. n = 3 embryos for each genotype. Mean ± s.d. NS, p > 0.05, one-way ANOVA test.
Scale bar: 50 μm in D, I, K, and M; 200 μm in P.

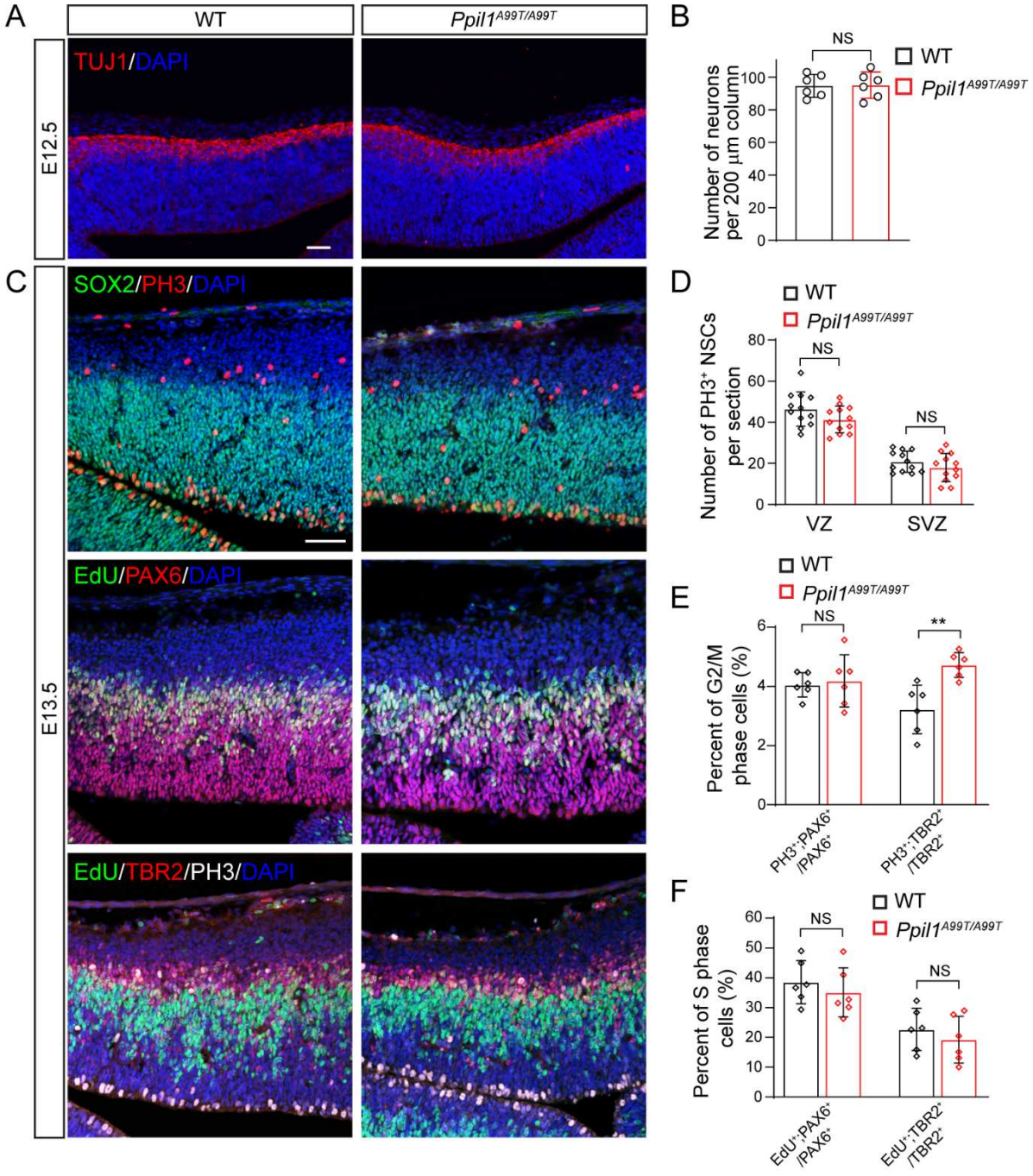

Figure S3. Cell cycle analysis of neural progenitor cells in developing *Ppil1*$^{A99T/A99T}$ brain cortex, related to Figure 3.

(A) Coronal sections of E12.5 brain cortex from WT and *Ppil1*$^{A99T/A99T}$ embryos stained for TUJ1 (red) and DAPI (blue).

(B) Quantification of TUJ1^{+} neurons per 200 μm column in E12.5 WT and *Ppil1*$^{A99T/A99T}$ brain cortex. n = 3 embryos for each genotype.

(C) Coronal sections of E13.5 brain cortex from WT and *Ppil1*$^{A99T/A99T}$ embryos stained for DAPI (blue) and top: SOX2 (green, NSCs) and PH3 (red, G2/M phase cells); middle: EdU (green, 0.5 hour pulse labeling, S phase cells) and PAX6 (red, NSCs); bottom: EdU (green, 0.5 hour pulse labeling), TBR2 (red, INPs), and PH3 (white).

(D) Quantification of PH3^{+} cells in ventricular zone (VZ) and subventricular zone (SVZ) per image in E13.5 WT and *Ppil1*$^{A99T/A99T}$ brain cortex. n = 3 embryos for each genotype. (E and F) Quantification of percent of G2/M (E) and S (F) phase cells in NSCs and INPs in E13.5 brain cortex. n = 3 embryos for each genotype.

Mean ± s.d. *p*-value: NS > 0.05; ** <0.005, unpaired t-test in B and one-way ANOVA test in D-F.

Scale bar: 50 μm.

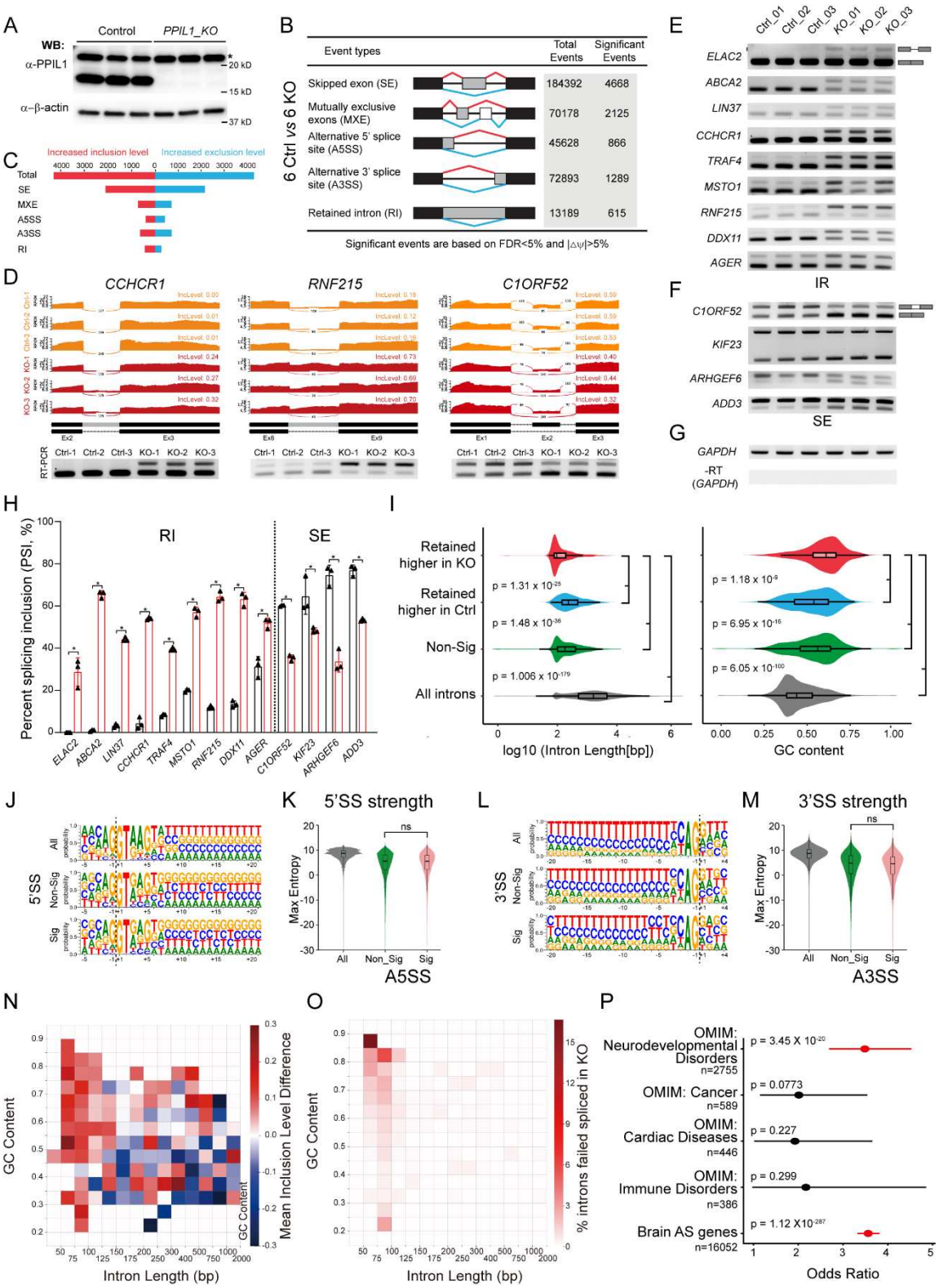

Figure S4. Knockout of *PPIL1* disrupts global splicing integrity in human HAP1 cells, related to Figure 4.

(A) Western blot showing the loss of PPIL1 protein expression in *PPIL1* knockout (KO) HAP1 cells. Asterisk indicates unspecific bands.

(B) Differential alternative splicing events in 6 *PPIL1* knockouts (KO) *vs.* 6 control HAP1 cell samples detected by rMATS. Black: constitutive exons, Gray: alternative exons. Red: inclusion types, Blue: exclusion types. Significant events based on FDR < 0.05; absolute inclusion level difference ($|\Delta\psi|$) > 5%.

(C) Columns showing numbers of significant events with higher inclusion level in *PPIL1* KO (red) or control cells (blue).

(D) Top: Sashimi plots of read density and the numbers of junctions for three representative genes in 3 *PPIL1* KO and 3 control samples. Bottom: RT-PCR verification. Intron retention (*CCHCR1* and *RNF215*) or exon skipping (*C1ORF52*).

(E-G) Validation of significant intron retention (E) and exon skipping (F) events by semi-quantitative RT-PCR using *GAPDH* as control (G, top). cDNA used for RT-PCR is free from genomic DNA contamination (F, below).

(H) Quantification of percent splicing inclusion (PSI) for RI and ES events identified in WT and *Ppil1* knockout HAP1 cells. PSI was calculated as percent of inclusion form transcripts among all transcripts (inclusion and exclusion forms) based on quantification of RT-PCR bands. n = 3 for each genotype. Mean ± s.d. * p <0.0001, one-way ANOVA test.

(I) Distribution of intron length and GC content among differentially spliced introns in WT and *PPIL1* KO cells. p-value: Wilcox test.

(J-M) Splice-site strength analysis of 5'SS (J and K) and 3'SS (L and M) in all introns (All, gray), non-significant A5SS or A3SS events (Non-sig, green), and significant A5SS or A3SS events (Sig, red) identified by rMATS in HAP1 cells. (J and L): Frequency distribution of nucleotides at consensus 5′SS (J) and 3′SS (L). (K and M): Strength of 5'SS (K) and 3'SS (M) calculated using Maxentpy. p-value: Wilcox test. Sig vs. All: $p < 1 \times 10^{-200}$ for 5'SS and $p < 1 \times 10^{-200}$ for 3'SS; Non_Sig vs. All: $p < 1 \times 10^{-200}$ for 5'SS and $p = 1.96 \times 10^{-128}$ for 3'SS; Sig vs. Non_Sig: $p = 0.373$ for 5'SS and $p = 0.353$ for 3'SS. Dash lines show where the splicing cleavage occurs.

(N) Heatmap showing mean inclusion level differences for subgroups of introns. Intron length (x-axis); GC content (y-axis). Red: higher inclusion in KO. Blue: higher inclusion in controls. Introns retained higher in KO were shifted to the top-left.

(O) Percent of introns that fail to splice in KO based upon intron length and GC content. Approximate 15% of retained introns with <75 bp and >85% GC showed significantly higher inclusion in KO.

(P) Mis-spliced genes in *PPIL1* KO cells were enriched for those listed as OMIM 'neurodevelopmental disorder' genes and 'brain alternatively spliced' (AS). Fischer's Exact test, Bonferroni corrected.

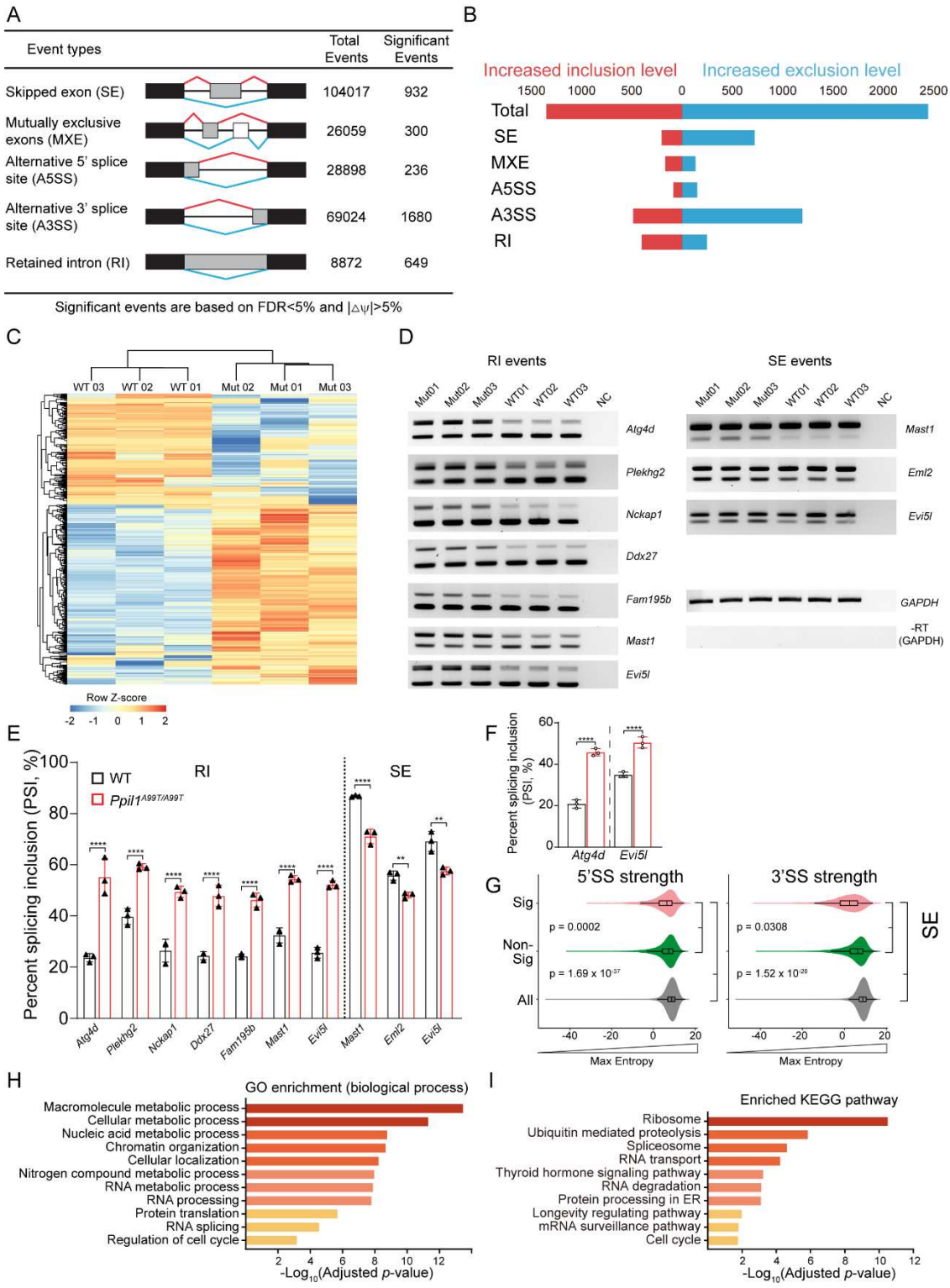

Figure S5. Defective alternative splicing in *Ppil1*$^{A99T/A99T}$ brains, related to Figure 4.
(A) Summary of different types of significant altered AS events identified from the comparison of 3 *Ppil1*$^{A99T/A99T}$ and 3 littermates WT E14.5 brain hemispheres using rMATS.

(B) Columns showing the numbers of significant events with higher inclusion level in *Ppil1*$^{A99T/A99T}$ (red) or in WT brains (blue).

(C) Heatmap showing the inclusion level of all the significant RI events in 3 *Ppil1*$^{A99T/A99T}$ and 3 littermates WT controls.

(D) Validation of significant RI and SE events in E14.5 mouse brains by semi-quantitative RT-PCR using *GAPDH* as control.

(E) Quantification of percent splicing inclusion (PSI) for RI and ES events identified in E14.5 WT and *Ppil1*$^{A99T/A99T}$ brains. PSI was calculated as percent of inclusion form transcripts among all transcripts (inclusion and exclusion forms) based on quantification of RT-PCR bands. n = 3 for each genotype. Mean ± s.d. *p*-value: ** <0.005, **** <0.0001, one-way ANOVA test.

(F) Quantification of percent splicing inclusion (PSI) for minigene splicing reporter assays in transfected WT and *Ppil1*$^{A99T/A99T}$ mouse embryonic fibroblasts. n = 3 for each genotype. Mean ± s.d. *p*-value: **** <0.0001, one-way ANOVA test.

(G) Splice-site strength analysis of 5'SS and 3'SS in all introns (All, gray), non-significant SE events (Non-sig, green), and significant SE events (Sig, red) identified by rMATS in mouse brains. The 5'SS and 3'SS strength show lower maximum entropy for choice points that were significantly different in KI compared with control. Wilcox test.

(H and I) Enrichment analysis of GO biological processes (H) and KEGG pathways (I) for misspliced genes (n = 2,134) among all expressed genes (n = 15,169) in E14.5 brains. Protein and RNA metabolic processes are mostly enriched, and cell cycle regulation is also significantly enriched.

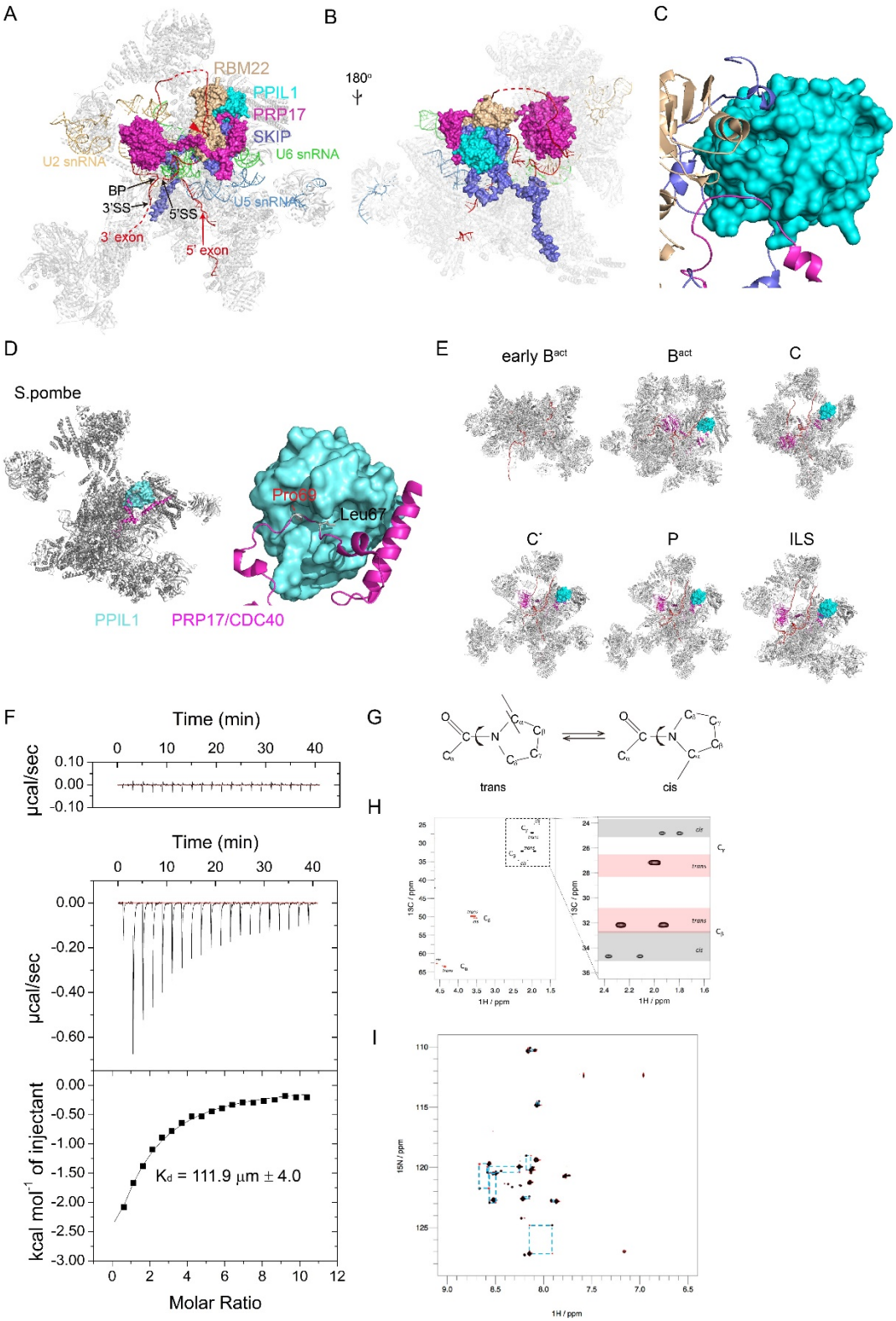

Figure S6. PPIL1 catalyzes PRP17 Gly94-Pro95 isomerization *in vitro*, related to Figure 5.

(A and B) Cryo-EM structure of spliceosome C* complex (PDB: 5XJC) highlighting PPIL1 (surface in teal) and its interacting proteins in the spliceosome, including PRP17 (purple), SKIP (slate blue), and RBM22 (orange). Pre-mRNA was labeled in red with missing region shown in red dash lines. In C* complex, U5 snRNA (light blue) binds to 5' exon, and U6 snRNA (green) forms a duplex with 5'SS. RMB22 binds to the intron downstream 5'SS, which traverses a positively charged channel (red arrowhead) within the N-terminal domain of RBM22. U2 snRNA (light orange) forms a duplex with branching point site (BPS) region which binds to the C-terminal WD40 domain of PRP17.

(C) Structures extracted from cryo-EM structure of spliceosome C* complex (PDB: 5XJC) showing the interactions between PPIL1 (surface in teal) and N-terminal domains of PRP17 (cartoon in purple), SKIP (cartoon in slate blue), and RBM22 (cartoon in orange). Binding to PPIL1 allows the association of these proteins in the activated spliceosome, and also induce a disorder-order transition for N-terminal domains of PRP17 and SKIP undergo disorder-order transition upon the binding to PPIL1.

(D) Cryo-EM structures of S. pombe ILS complex (PDB: 3JB9) show an N-terminal loop of PRP17 (cartoon in purple) bound to the PPIL1 (teal) enzymatic surface with Pro69 buried inside the S1 enzymatic pocket (Yan et al., 2015a).

(E) Cryo-EM structures of human spliceosomal complexes showing the binding of PRP17 (cartoon in purple) to PPIL1 (surface in teal). The spliceosomal complexes shown include early B^{act} (PDB: 5Z58), B^{act} (PDB: 5Z56), C (PDB: 5YZG), C* (PDB: 5XJC), P (PDB: 6QDV), and ILS (PDB: 6ID0) (Fica et al., 2019; Zhan et al., 2018a; Zhang et al., 2017; Zhang et al., 2018; Zhang et al., 2019). Pro95 was observed inside the active site of PPIL1 in B^{act}, C, C*, P, and ILS.

(F) Isothermal titration calorimetry (ITC) analysis for the binding affinity between PPIL1 and PRP17 peptide (aa 89-101: FAPEFG[P]ENPFRT). PRP17 peptide (2 mM) was titrated into PPIL1 (40 μM) at 25 oC in PBS (pH = 7.4). Top: Control titration of PRP17 peptide into the buffer, to determine the heat of dilution. Middle: Sequential heat pulse data for the titration of PRP17 peptide into PPIL1 protein. (Bottom) PPIL1 and PRP17 peptide-binding curve, showing integrated heat changes upon binding. Curve fitting with a fixed stoichiometry of 1.0 was used to calculate the Kd of this interaction (111.9 μM ± 4.0).

(G) Schematic view of imide peptide bond preceding a proline residue, which can exist as both trans and cis conformation depending on the Cα atoms of the two amino acids are on the same or opposite side of the peptide bond, respectively.

(H) Assignment of major and minor resonances of PRP17 peptide (aa 89-101 with P95 13C and 15N double labeled) using a 1H 13C HSQC spectrum. 1H 13C HSQC spectra show H-C correlations, which in proline correspond to α, β, γ, and δ C-H (left). The HSQC spectrum shows major and minor signals corresponding to trans and cis peptide bond isomers, respectively. The major and minor states were assigned based on 13Cβ and 13Cγ chemical shifts (right), which show greater chemical shift difference in the cis state

compared to the trans-state (as described by (Shen and Bax, 2010)). Expected 13Cβ and 13Cγ shifts for trans (pink) and cis (grey) isomers are shaded on the enlarged 13Cβ and 13Cγ region of the spectrum (mean ± one standard deviation; (Shen and Bax, 2010)). (I) ZZ exchange spectroscopy showing catalyzed proline isomerization of uniformly 15N labeled PRP17 peptide by PPIL1. 1H 15N ZZ exchange NMR spectra (with a 150 ms mixing time) were recorded in the presence (red) or absence (black) of catalytic concentrations of PPIL1. Upon addition of PPIL1, new exchange signals appear between the major (trans) and minor (cis) signals of PRP17, shown with dashed blue connecting lines.

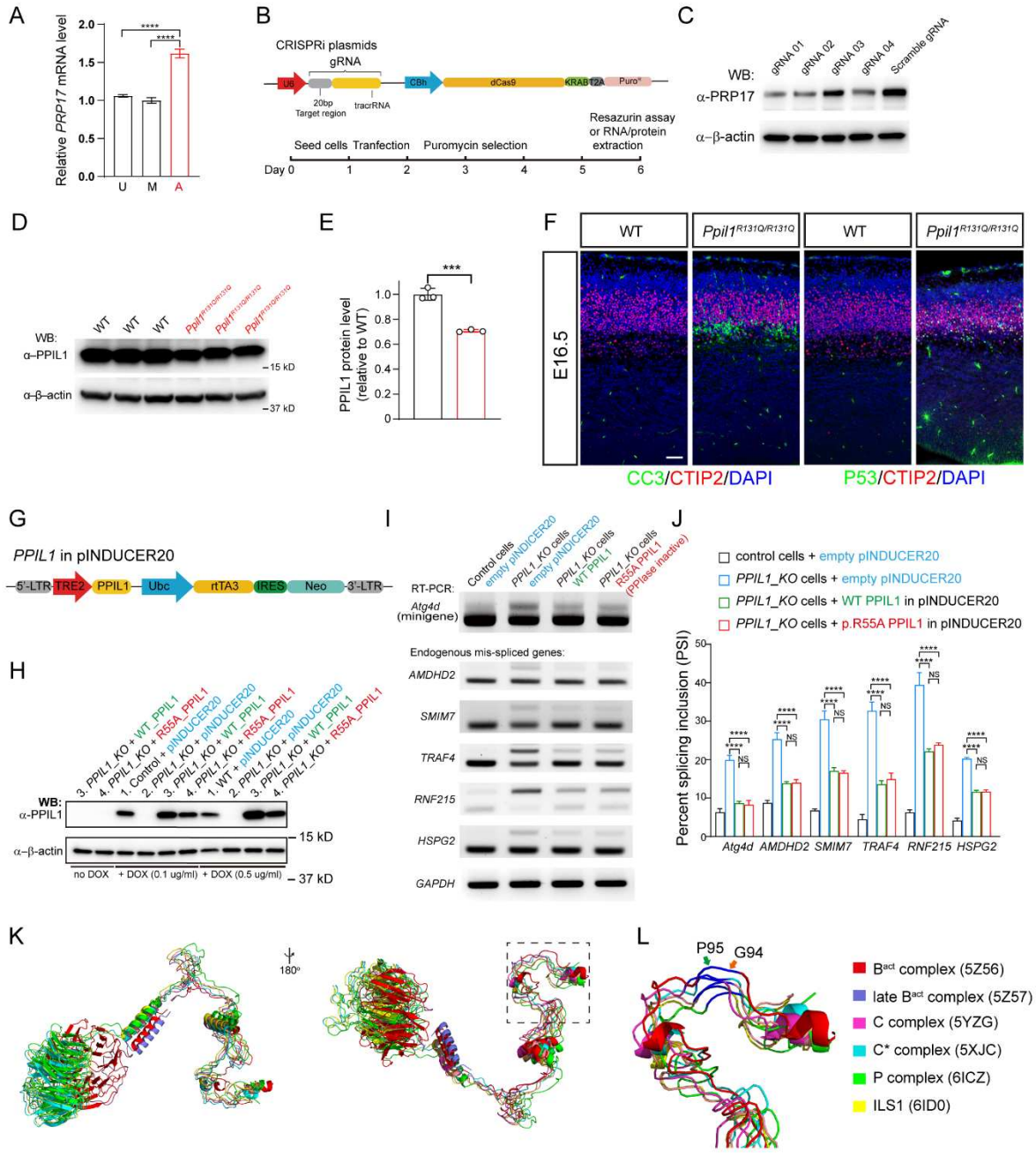

Figure S7. PPIL1 and PRP17 regulate RNA splicing independent of proline isomerization, related to Figure 6.

(A) RT-qPCR quantification of *PRP17* mRNA expression levels in human fibroblast cells. n = 3 per samples. Mean ± s.d. *p*-value: **** <0.0001, one-way ANOVA test.

(B) CRISPRi DNA construct allowing for dCas9-KRAB mediated transcriptional repression of *PRP17*, and the timeline of experiments performed in HEK293T cells.

(C) Reduced PRP17 expression using CRISPRi showing the most potent repression with gRNA 01.

(D and E) Western blot analysis (D) and quantification (E) of endogenous PPIL1 protein in E14.5 WT and *Ppil1*$^{R131Q/R131Q}$ embryos. n = 3 for each genotype, *** p = 0.0005, unpaired t-test.

(F) Coronal sections of E16.5 brain cortex from WT and *Ppil1*$^{R131Q/R131Q}$ embryos stained for DAPI (blue), CC3 (green, left), P53 (green, right), and CTIP2 (red). Scale bar: 50 μm.

(G) Schematic view of DNA construct with *PPIL1* in Doxycycline (Dox)-inducible lentiviral vector pInducer20.

(H) Western blot showing DOX-induced expression of WT or p.R55A PPIL1 in control and *PPIL1* KO HAP1 cells. Genotypes of the cells used are labeled in black and lentivirus vectors used are labeled in color.

(I) Rescue of RNA splicing defects in *PPIL1* KO HAP1 cells after lentiviral transduction of WT or p.R55A PPIL1 rescue splicing defects for *Atg4d* minigene and for endogenous misspliced genes.

(J) Quantification of percent splicing inclusion (PSI) for *Atg4d* minigene splicing reporter and selective RI events in HAP1 cells. n = 3 for each condition. Mean ± s.d. p-value: NS > 0.05; * <0.05; ** <0.005; *** <0.001; **** <0.0001, one-way ANOVA test.

(K and L) Structures of PRP17 extracted from the cryo-EM structures of different spliceosomal complexes, including B^{act}, late B^{act}, C, C*, P, ILS1, and ILS complexes **(Fica et al., 2019; Zhan et al., 2018a; Zhang et al., 2017; Zhang et al., 2018; Zhang et al., 2019)** showing a consistent trans conformation for PRP17 Gly94-Pro95 bond. (L) Magnification of the dashed region. PDB numbers were shown in the panel.

Table S1. Clinical information of all the affected individuals, related to Table 1

	Family 1		Family 2	Family 3		Family 4	Family 5		Family 6	Family 7	Family 8		Family 9		PRP17 Family 10
	IV:1	IV:3	IV:6	III:1	III:3	III:3	III:1	III:2	II:1	II:1	II:1	II:2	II:1	II:2	V:3
Mutation gDNA (hg19)	chr6:g.36823795C>T	chr6:g.36823795C>T	chr6:g.36823795C>T	chr6:g.36823771T>C	chr6:g.36823771T>C	chr6:g.36824409T>C	chr6:g.36823698C>T	chr6:g.36823698C>T	chr6:g.[36823772_36823789dup; 36823765C>A]	chr6:g.[36824397A>G]; [36823698C>T]	chr6:g.[36823711T>C]; [36824361C>T]	chr6:g.[36823711T>C]; [36824361C>T]	chr6:g.[36823711T>C]; [36839572G>A]	chr6:g.[36823711T>C]; [36839572G>A]	PRP17 hg19:chr6:110550122T>G
Mutation cDNA (PPIL1 NM_016059.1, PRP17 NM_015891.2)	c.295G>A	c.295G>A	c.295G>A	c.319A>G	c.319A>G	c.233A>G	c.392G>A	c.392G>A	c.[301_318dup; 325G>T]	c.[245T>C]; [392G>A]	c.[379A>G]; [280+1G>A]	c.[379A>G]; [280+1G>A]	c.[379A>G];[133C>T]	c.[379A>G];[133C>T]	c.1505T>G
Mutation Protein (PPIL1 NP_057143.1, PRP17 NP_056975.1)	p.Ala99Thr	p.Ala99Thr	p.Ala99Thr	p.Thr107Ala	p.Thr107Ala	p.Tyr78Cys	p.Arg131Gln	p.Arg131Gln	p.[Ala101_Asp106dup; Gly109Cys]	p.[Phe82Ser; Arg131Gln]	p.[Thr127Ala];[?]	p.[Thr127Ala];[?]	p.[Thr127Ala]; [Arg45*]	p.[Thr127Ala]; [Arg45*]	p.Phe502Cys
Gender	Male	Male	Female	Male	Female	Female	Female	Male	Female	Male	Female	Male	Male	Female	Female
Ethnic origin	Egyptian	Egyptian	Egyptian	Pakistani	Pakistani	Mexican	Egyptian	Egyptian	Pakistani	Chinese	European-American	European-American	European-American	European-American	Egyptian
Parental consanguinity	+	+	+	+	+	+	+	+	+	-	-	-	-	-	+
Pregnancy duration	full term	full term	Full term	full term	full term	full term	full term	full term	full term	full term	full term	full term	full term	full term	full term
Weight at birth (kg)	1.75kg	2.5kg	2.9kg	1.8kg	2.0kg	2.8kg	2.3kg	2.7kg	1.7kg	3.0kg	4.1kg	3.7kg	3.3kg	3.4kg	2.6kg
Length at birth (cm)	N/A	50cm	49cm	45cm	46cm	61cm	N/A	N/A	48cm	N/A	48cm	52cm	51cm	51cm	48cm
Head circumference at birth (SD)	28cm (-6SD)	28cm (-6SD)	28cm (-5 SD)	30cm (-4SD)	30cm (-4SD)	28cm (-4.5SD)	29cm (-4SD)	29cm (-3SD)	30cm (-4SD)	30cm (-2.5SD)	29cm (-4SD)	29cm (-3SD)	32cm (-2SD)	32cm (-2SD)	30cm (-3SD)
HC at last examination (SD)	36cm (-8SD) at 9 mos	36cm (-8SD) at 9 mos	30cm (-7 SD) at 2 mos	39cm (-5SD) at 1 y	39cm (-5SD) at 1 y	36cm (-8SD) at 9 mos	37cm (-6SD) at 9 mos	43cm (-4SD) at 2 y	39cm (-5SD) at 1 y	45cm (-4SD) at 4 y	43cm (-8SD) at age 10 y	42cm (-5SD) at 2 y	45.5cm (-6SD) at 13 y	43cm(-7SD) at 8 y	42 cm (-5SD) at 4y
Intellectual Disability	Severe	Severe	delayed	Severe	Severe	Severe	Severe	Severe	Severe	Severe	Severe	Severe	Severe	Severe	Severe
Development															
Gross motor (normal/delayed/absent)	Absent	Absent	delayed	Absent	Absent	Absent	Delayed	Delayed	Absent	Delayed	Absent	Absent	Absent	Absent	Delayed
Fine motor (normal/delayed/absent)	Absent	Absent	deayed	Absent	Absent	Absent	Absent	Absent	Absent	Delayed	Absent	Absent	Absent	Absent	Absent
Language (normal/delayed/absent)	Absent	Absent	-	Absent	Absent	Absent	Absent	Absent	Absent	Delayed	Absent	Absent	Absent	Absent	Absent
Social (normal/delayed/absent)	Absent	Absent	delayed	Absent	Absent	Absent	Absent	Absent	Absent	Delayed	Absent	Absent	Absent	Absent	Absent
Seizures															
Onset	Birth	Newborn	1.5m	-	-	Infancy	Infancy	Infancy	-	Infancy	Infancy	Infancy	Infancy	Infancy	Infancy
Type	Focal	Myoclonic	myoclonic/focal	-	-	Focal	Generalized	Myoclonic	-	Myoclonic	Infantile spasms	Infantile spasms	Infantile spasms	Myoclonic / GTC	Myoclonic / GTC
Frequency	Intractable	Intractable	fairly controlled on levteracetum	-	-	Infrequent	Infrequent	Monthly	-	Monthly	Intractable	Intractable	Daily, Intractable	Intractable	Intractable
Neurological Findings															
Hypertonia	Mild	Mild	mild	-	-	-	Mild	Mild	-	-	Mild	Mild	Mild	Mild	Mild
Hypotonia	-	-	-	Severe	Severe	Severe	Mild	Mild	Severe	-	Mild	Mild	Mild	Mild	-
Deep tendon reflexes	Brisk	Brisk	present/brisk	Brisk	Brisk	Brisk	Brisk	Brisk	Brisk	-	Brisk	Brisk	Brisk	Brisk	Brisk
Spastic tetraplegia	+	+	+	+	+	+	+	+	++	-	+	+	+	+	+
Investigations															
Metabolic testing	-	-	normal	-	-	-	-	-	-	-	-	-	-	-	-
EEG	High voltage disorganized	High voltage disorganized	slow waves, disorganized	N/A	N/A	High voltage disorganized	High voltage disorganized	High voltage disorganized	N/A	High voltage disorganized	High voltage disorganized	Hypsarrhythmia	Hypsarrhythmia	High voltage disorganized	Generalized spike and wave
Brain Imaging															
Pontocerebellar hypoplasia	+	+	+	+	+	+	+	+	+	+	+	+	+	+	+
Simplified cortical gyral patterning	+	+	+ and increase extraaxial CSF	-	-	+	-	-	-	-			-	-	-
Agenesis of corpus callosum	+	+	partial	+	+	Partial	+	+	+	Partial			Partial	Partial	Partial
Cerebellar hypoplasia	+	+	+	+	+	+	+	+	+	+	+	+	+	+	+
Brainstem hypoplasia	+	+	+	+	+	+	+	+	+	+	+	+	+	+	+
Hydrocephalus	-	-	-	-		-	-	-	+	-			-	-	-
White matter abnormalities	-	-	defective myelination more than being corresponding to age	-	-	Delayed myelination	-	-	-	-			Delayed myelination	-	-
Other															
	Died at 8mos			Died at 2mo	Died at 3 mo	Dystonia			Died at 2 mo	Dystonia	Dystonia	Dystonia			
	Inguinal hernia			Persistent thrombocytopaenia	Persistent thrombocytopaenia	Chronic neutropenia				Chronic neutropenia					Chronic anemia and thrombocytopenia

Table S2. Clinical variants table

Family	Chr	Start	End	Ref	Alt	Gene	Transcript	cDNA	AAChange	OMIM	Zygosity	Function	Impact	LocalAF	GnomAD_AF	CADD_PHRED	MutTaster	SIFT	PolyPhen	Notes
1	2	131520015	131520015	C	T	AMER3	NM_001105193.1	c.370C>T	p.(Arg124Trp)		hom	missense_variant	MODERATE	0.000213432	0.0000325	33	polymorphism	deleterious(0)	possibly_damaging(0.744)	wtx/amer2/amer3 triple mutant zebrafish developed normally, were fertile and did not
	6	31118815	31118815	G	C	CCHCR1	NM_001105563.1	c.778C>G	p.(Leu260Val)	605310	hom	missense_variant	MODERATE	0.00035572	0	21.8	polymorphism	tolerated(0.11)	possibly_damaging(0.883)	Many people in GnomAD database showed homozugous null mutations without pher
	6	33052835	33052835	G	A	HLA-DPB1	NM_002121.5	c.473G>A	p.(Trp158*)	142858	hom	stop_gained	HIGH	0.000569152	0	36	disease_causing_automatic	-	-	A component in major histocompatibility complex, unlikely cause brain disease
	6	36823795	36823795	C	T	PPIL1	NM_016059.4	c.295G>A	p.(Ala99Thr)	601301	hom	missense_variant	MODERATE	0.000284576	0.0000142	26	disease_causing	deleterious(0.04)	benign(0.007)	Modeled in mice in this study
Family	**Chr**	**Start**	**End**	**Ref**	**Alt**	**Gene**	**Transcript**	**cDNA**	**AAChange**	**OMIM**	**Zygosity**	**Func**	**Impact**	**LocalAF**	**GnomAD_AF**	**CADD_PHRED**	**MutTaster**	**SIFT**	**PolyPhen**	**Notes**
3	6	36823771	36823771	T	A	PPIL1	NM_016069.4	c.319T>A	p.Thr107Ala	601301	hom	missense_variant	MODERATE	0.00029	0	29.7	disease_causing	deleterious(0)	possibly_damaging(0.821)	Modeled in mice in this study
Family	**Chr**	**Start**	**End**	**Ref**	**Alt**	**Gene**	**Transcript**	**cDNA**	**AAChange**	**OMIM**	**Zygosity**	**Func**	**Impact**	**LocalAF**	**GnomAD_AF**	**CADD_PHRED**	**MutTaster**	**SIFT**	**PolyPhen**	**Notes**
4	6	36824409	36824409	T	C	PPIL1	NM_016059.4	c.233A>G	p.Y78C	601301	hom	missense_variant	MODERATE	0.00013	0	26.6	disease_causing	deleterious(0)	probably_damaging(0.979)	
	8	65527712	65527712	G	A	CYP7B1	NM_004820.3	c.928C>T	p.R310W	603711	hom	missense_variant	MODERATE	0.00014	0.00002391	32	polymorphism	tolerated(0.07)	probably_damaging(0.969)	Biallelic loss causes a different disease (Spastic Paraplegia)
Family	**Chr**	**Start**	**End**	**Ref**	**Alt**	**Gene**	**Transcript**	**cDNA**	**AAChange**	**OMIM**	**Zygosity**	**Func**	**Impact**	**LocalAF**	**GnomAD_AF**	**CADD_PHRED**	**MutTaster**	**SIFT**	**PolyPhen**	**Notes**
5	6	36823698	36823698	C	T	PPIL1	NM_016059.4	c.392G>A	p.(Arg131Gln)	601301	hom	missense_variant	MODERATE	0.000284576	0.0000495	34	disease_causing	tolerated(0.06)	possibly_damaging(0.518)	
Family	**Chr**	**Start**	**End**	**Ref**	**Alt**	**Gene**	**Transcript**	**cDNA**	**AAChange**	**OMIM**	**Zygosity**	**Func**	**Impact**	**LocalAF**	**GnomAD_AF**	**CADD_PHRED**	**MutTaster**	**SIFT**	**PolyPhen**	**Notes**
9	6	32069018	32069018	C	T	TNXB	NM_019105.6	c.5706G>A	p.Met1902Ile	600985	het	missense_variant	MODERATE	0.00079	0	11	polymorphism	tolerated	benign	Predicted as non-damaging by all MutTaster, SIFT, and PolyPhen
	6	32068536	32068536	T	A	TNXB	NM_019105.6	c.6074A>T	p.Asp2025Val	600985	het	missense_variant	MODERATE	0.0011	0.000586	23	disease_causing	damaging	probably_damaging(0.916)	
	6	36855935	36855935	T	C	PPIL1	NM_016069.4	c.379A>G	p.Thr127Ala	601301	het	missense_variant	MODERATE	0.00079	0.0000667	22	disease_causing	damaging	benign	
	6	36871796	36871796	G	A	PPIL1	NM_016069.4	c.133C>T	p.Arg45Ter	601301	het	stop_gained	HIGH	0.00098	0	37	disease_causing			
Family	**Chr**	**Start**	**End**	**Ref**	**Alt**	**Gene**	**Transcript**	**cDNA**	**AAChange**	**OMIM**	**Zygosity**	**Func**	**Impact**	**LocalAF**	**GnomAD_AF**	**CADD_PHRED**	**MutTaster**	**SIFT**	**PolyPhen**	**Notes**
10	2	37234206	37234206	C	T	HEATR5B	NM_019024.2	c.4764G>A	p.(Met1588Ile)		hom	missense_variant	MODERATE	0.000142288	0	24.1	disease_causing	deleterious(0.03)	benign(0.037)	Did not segregate
	6	110550122	110550122	T	G	CDC40/PRP17	NM_015891.2	c.1505T>G	p.(Phe502Cys)	605585	hom	missense_variant	MODERATE	0.000142288	0.000008191	31	disease_causing	deleterious(0.02)	probably_damaging(1)	
	11	68191092	68191092	G	C	LRP5	NM_002335.3	c.3163G>C	p.(Gly1055Arg)	603506	hom	missense_variant	MODERATE	0.000213432	0	25.2	disease_causing	deleterious(0)	probably_damaging(0.916)	Biallelic loss causes a different disease (bone defects)
	11	68517700	68517700	C	T	TESMIN	NM_001039656.1	c.429G>A	p.(Trp143*)	604374	hom	stop_gained	HIGH	0.000142288	0	35	disease_causing_automatic	-	-	Not expressed in brain, knockout mice exhibited male infertility without brain defects
	11	110104002	110104002	G	A	RDX	NM_001260492.1	c.1547C>T	p.(Thr516Ile)	179410	hom	missense_variant	MODERATE	0.000142288	0.00004375	31	disease_causing	deleterious(0.01)	probably_damaging(0.999)	Biallelic loss causes a different disease (deafness) when mutated

1. Identified variants from WES/WGS were filtered if not consistent with recessive monogenic inheritance, if the minor allele frequency (MAF) of gnomAD was >1:10,000, if MAF of local cohort was > 1:1,000, if not moderate or high impact, if CADD PHRED score ≤20, or if not predicted as damaging by either SIFT, PolyPhen, or MutationTaster.
2. WES were performed for two affected inviduals in Family 5 and 9, and only shared variants were considered.

Chr	Chromosome
Start	Start coordinate of the target region (probe). Genomic position.
End	Stop coordinate of the target region (probe).
Ref	Reference allele
Alt	Alternate allele
Gene	HGNC symbol of the gene where the target region is located.
cDNA	cDNA change as determined from the transcript, in HGVS notation
AAChange	Amino acid change as determined from the transcript, in HGVS notation
OMIM	OMIM ID of the gene where the target region is located.
Function	Variant effect name as defined in the Sequence Ontology (SO)
Impact	Putative Impact based on Sequence Ontology terms (MODIFIER, LOW, MODERATE, HIGH).
LocalAF	Matches of the variant in the local database as fraction of detections / total number of persons in the local database.
GnomAD_AF	Population frequency from the merged exome + genome data set of the gnomAD database.
CADD_PHRED	The Combined Annotation Dependent Depletion score of predicted deleteriousness of the variant.
MutTaster	Mutation Taster predicted amino acid substitution impact on protein function.
Sift	SIFT predicted amino acid substitution impact on protein function.
PolyPhen	PolyPhen-2 predicted amino acid substitution impact on protein function.

Table S3. Summary of altered RNA splicing events in *PPIL1* KO HAP1 cells using rMATS and Leafcutter

rMATS

	6 KO vs. 6 Ctrls		3 KO vs. 3 Ctrls		3 Ctrls vs. 3 Ctrls		3 KO vs. 3 KO	
Events types	Total	Significant	Total	Significant	Total	Significant	Total	Significant
SE	184392	4668	123757	4275	114584	1653	128772	2018
RI	13189	615	10382	702	10040	273	10417	326
A5SS	45628	866	31408	831	29772	466	32059	513
A3SS	72893	1289	48504	1356	45638	909	49948	1003
MXE	70178	2125	36144	1438	31816	744	38447	979
Total	386280	9563	250195	8602	231850	4045	259643	4839

Leafcutter

	6 KO vs. 6 Ctrls		3 KO vs. 3 Ctrls		3 Ctrls vs. 3 Ctrls		3 KO vs. 3 KO	
Events types	Total	Significant	Total	Significant	Total	Significant	Total	Significant
3'/5'SS	10609	530	9844	140	9859	0	9872	0
SE	969	118	935	47	817	0	890	0
IE/NE	1252	191	1027	72	754	0	767	0
Others	20285	2002	21309	698	21685	8	21586	0
Total	33115	2841	33115	957	33115	8	33115	0

Table S4. Summary of the eight cyclophilin PPIases in the spliceosomal complexes

Spliceosomal PPIase	Spliceosomal complexes association	Putative substrate	References
PPIH	B	-	(Agafonov et al., 2011; Bessonov et al., 2010; Fica et al., 2019; Haselbach et al., 2018; Rappsilber et al., 2002; Teigelkamp et al., 1998; Zhan et al., 2018a, b; Zhang et al., 2017; Zhang et al., 2018; Zhang et al., 2019; Zhou et al., 2002)
CWC27	B^{act}	-	
PPIE	B^{act}, B*, C, C*, P, ILS	-	
PPIL1	B, B^{act}, B*, C, C*, P, ILS	PRP17	
PPIL2	B, B^{act}, B*, C	-	
PPIL3	C	-	
PPIG	C	-	
PPWD1	C	-	

Green letters indicate observation in the cryo-EM structures

Table S5. Primer Sequences for RT-PCR, Related to Method Details			
Purpose	Name	Forward	Reverse
Validation of RI events in human HAP1 cells	ELAC2	CCTCAGTTCACAACCTTCGC	GGAGCTGGTACTTGAGGAGG
	ABCA2	CTGTTTGTGTTCGACCTGCC	GACAATGAGGAACACGTAGGC
	LIN37	CCTCACCCTCCACACTCATC	AGTAACGAAGCTGGTTCCGA
	CCHCR1	AGAGCCTTCAAATAATGTGGAGA	CCGCCTCTCTGAGACATCTT
	TRAF4	CCTATCCGCTGCATCCACA	CTTCATGGGGCAGCGATTAG
	MSTO1	GGACAGGCTGCATTTCTACG	CAGAGAAGCCATCGTGCAG
	hsRNF215-F	GAGACTGTGTGGACCCCTG	TGGGCAGCTAATCATCGGAG
	DDX11	GCTCCTGGACCAGCGATAT	CAGGCAGTGGTGTGGTTG
	ACER	TGTGTCAGAGGGAAGCTACC	AGTGTGAAGAGCCCTGTCTC
Validation of SE events in human HAP1 cells	C1ORF52	GCCCGGCCTTTCTCTACAAT	GAGGCTTCTTCTCAGTGGTG
	KIF23	CAGCTGGAGATGCAGAATAAACT	GAATTGGTGGTGCGTTCTGA
	ARHGEF6	ACCGTGGAGTTTAAGTTGTCT	ACATATTCCTCCTCCGATGGT
	ADD3	CACCAGCTCCTCCTAACCC	TGCTTAACCTACTCACTCGCT
RT-PCR control in human HAP1 cells	GAPDH	AGGGCTGCTTTTAACTCTGGT	CCCCACTTGATTTTGGAGGGA
Validation of RI events in mouse brains	Atg4d	TCGGTCTACATCGGCTAGTG	TGAGAGACGTACACCACCAG
	Plekhg2	CTCCATCTCCAAGACTTTCTGGCA	CATTCTGGGGAAAAATGACATAAGCTTC
	Nckap1	AAGGCGTGGATATTCTCGGT	GCTGTCCCGGATTGAAGAAC
	Ddx27	AGAAGAAGAAGAAGAAGGGCCA	ACAGGCTTTTGTCATACTCGG
	Fam195b	GTGTGCCGGTGTGAAAATCT	CCAAGCACTAGGACTGGACA
	Mast1	CCCCGATACATCATCCGACA	CAGATGTGTCGTCTTGCTCC
	Evi5l	AGGAAGTGATGGCTGTTCGA	GGATGTACTGCGATGAATCCG
Validation of SE events in mouse brains	Mast1	AGTTTCTTCCGAGACCTGGA	GCTGCTCCATACTGCTGTAC
	Eml2	TGGACACAGAGACCCATGAC	CAGGTGGGTGATAAAACTGGA
	Evi5l	ACAGCGGATTGAGACCCTAG	GAAGGTCCTCTGCAGTCGAG
RT-PCR control in mouse brains	GAPDH	CATGGCCTTCCGTGTTCCTA	CCTGCTTCACCACCTTCTTGAT
Minigene splicing assay	Pspliceexpress	CTCTCTACCTGGTGTGTGGG	AGTGCCAAGGTCTGAAGGTC